Kaunas University of Technology
Faculty of Mathematics and Nature Sciences

Mathematical Model of Photopolymer Curing

Master's Final Degree Project

Julius Čeponis
Project author

Assoc. Prof. Dr. Mantas Landauskas
Supervisor

Kaunas, 2026

Kaunas University of Technology
Faculty of Mathematics and Nature Sciences

Mathematical Model of Photopolymer Curing

Master's Final Degree Project
Data Science and Artificial Intelligence (6211AX013)

Julius Čeponis
Project author

Assoc. Prof. Dr. Mantas Landauskas
Supervisor

Assoc. Prof. Dr. Rasa Šmidtaitė
Reviewer

Kaunas, 2026

Kaunas University of Technology

Faculty of Mathematics and Nature Sciences

Julius Čeponis

Mathematical Model of Photopolymer Curing

Declaration of Academic Integrity

I confirm the following:

1. I have prepared the final degree project independently and honestly without any violations of the copyrights or other rights of others, following the provisions of the Law on Copyrights and Related Rights of the Republic of Lithuania, the Regulations on the Management and Transfer of Intellectual Property of Kaunas University of Technology (hereinafter – University) and the ethical requirements stipulated by the Code of Academic Ethics of the University;

2. All the data and research results provided in the final degree project are correct and obtained legally; none of the parts of this project are plagiarised from any printed or electronic sources; all the quotations and references provided in the text of the final degree project are indicated in the list of references;

3. I have not paid anyone any monetary funds for the final degree project or the parts thereof unless required by the law;

4. I understand that in the case of any discovery of the fact of dishonesty or violation of any rights of others, the academic penalties will be imposed on me under the procedure applied at the University; I will be expelled from the University and my final degree project can be submitted to the Office of the Ombudsperson for Academic Ethics and Procedures in the examination of a possible violation of academic ethics.

Julius Čeponis

Confirmed electronically

Čeponis, Julius. Mathematical Model of Photopolymer Curing. Master's Final Degree Project / supervisor Assoc. Prof. Dr. Mantas Landauskas; Faculty of Mathematics and Nature Sciences, Kaunas University of Technology.

Study field and area (study field group): Applied Mathematics (Mathematical Sciences)

Keywords: photopolymer curing, function fitting, particle swarm optimization, grey-box modelling

Kaunas, 2026. 56 p.

Summary

Stereolithography is an additive manufacturing technique that fabricates three-dimensional objects with high speed and precision by selectively exposing a liquid photopolymer using a laser beam. It is most commonly applied in prototyping and the production of medical devices and implants. To achieve highly dimensional accuracy, stereolithography processes are typically described using physical models, chemical kinetic models, or hybrid approaches, while certain aspects of the process can also be optimized using machine learning. However, under high exposure conditions, the experimentally observed relationship between exposure and photopolymer cure depth – known as the working curve – occasionally deviates from classical models. One proposed mechanism for this deviation is the optical bleaching phenomenon: as the photopolymer cures, its optical properties change, allowing greater light penetration and increasing the exposure received by the uncured material. In this thesis, a data-driven approach is developed that extends a classical physics-based model to account for optical bleaching, and the model is validated using real experimental data. The extended model uses four parameters that are optimized in a two-stage function fitting process. Two parameters, identical to those in the original model, are extracted from the linear portion of the data, while two additional parameters are optimized from the full data. The performance of the extended model was evaluated using two experimental datasets comprising a total of 75 experiments. For fully linear experiments, both models achieved similar accuracy, indicating that the extended model does not deviate from the original formulation under normal conditions. For super-logarithmic cases, where the working curve increases at higher exposures, the extended model consistently outperformed the baseline. However, for the sub-logarithmic cases, where the working curve decreases with higher exposures, the extended model underperformed relative to the original model. These results indicate that optical bleaching effectively captures only the super-logarithmic behavior of the working curve. Finally, the consistency of the extended model was evaluated using three similar experiments, demonstrating that the model remains relatively stable under comparable conditions.

Čeponis, Julius. Fotopolimerų stingimo matematinis modelis. Magistro baigiamasis projektas / vadovas doc. dr. Mantas Landauskas; Kauno technologijos universitetas, Matematikos ir gamtos mokslų fakultetas.

Studijų kryptis ir sritis (studijų krypčių grupė): Taikomoji matematika (matematikos mokslai).

Reikšminiai žodžiai: fotopolimerų stingimas, funkcijos pritaikymas, dalelių spiečiaus optimizavimas, pilkosios dėžės modeliavimas

Kaunas, 2026. 56 p.

Santrauka

Stereolitografija yra adityviosios gamybos technologija, leidžianti dideliu greičiu ir tikslumu gaminti trimates struktūras, selektyviai apšviečiant skystą fotopolimerą lazerio spinduliu. Ši technologija dažniausiai taikoma prototipų kūrimui bei medicininių prietaisų ir implantų gamybai. Siekiant didelio matmenų tikslumo, stereolitografijos procesai paprastai aprašomi fizikiniais modeliais, cheminės kinetikos modeliais arba hibridiniais metodais, o tam tikri proceso aspektai taip pat gali būti optimizuojami taikant mašininį mokymąsi. Tačiau esant didelėms apšvitos dozėms, eksperimentiškai stebimas ryšys tarp apšvitos ir fotopolimero sukietėjimo gylio – vadinamoji darbinė kreivė – kartais nukrypsta nuo klasikinių modelių prognozių. Vienas iš siūlomų šio nukrypimo mechanizmų yra optinio balinimo reiškinys: fotopolimerui kietėjant, kinta jo optinės savybės, leidžiančios šviesai prasiskverbti giliau ir padidinančios nepakietėjusios medžiagos gaunamą apšvitą. Šiame darbe sukurtas duomenimis grįstas metodas, kuris išplečia klasikinį fizika pagrįstą modelį, įtraukiant optinio balinimo efektą, o modelis patvirtinamas naudojant realius eksperimentinius duomenis. Išplėstinis modelis naudoja keturis parametrus, kurie optimizuojami taikant dviejų etapų funkcijų pritaikymo procesą. Du parametrai, tapatūs pradinio modelio parametrams, nustatomi iš tiesinės duomenų srities, o du papildomi parametrai optimizuojami naudojant visą duomenų rinkinį. Išplėstinio modelio veikimas buvo įvertintas naudojant du eksperimentinius duomenų rinkinius, apimančius iš viso 75 eksperimentus. Visiškai tiesinių eksperimentų atveju abu modeliai pasiekė panašų tikslumą, kas rodo, jog išplėstinis modelis įprastomis sąlygomis nenukrypsta nuo pradinės formuluotės. Superlogaritminiais atvejais, kai darbinė kreivė didėja esant didesnėms apšvitoms, išplėstinis modelis pranoko bazinį modelį. Tačiau sublogaritminiais atvejais, kai darbinė kreivė mažėja didėjant apšvitai, išplėstinis modelis pasirodė prasčiau nei originalus modelis. Šie rezultatai rodo, kad optinio balinimo efektas efektyviai aprašo tik superlogaritminį darbinės kreivės elgesį. Galiausiai, išplėstinio modelio nuoseklumas buvo įvertintas naudojant tris panašius eksperimentus, parodant, kad modelis išlieka gana stabilus esant panašioms sąlygoms.

Table of contents

List of figures

List of tables

List of abbreviations and notations

Abbreviations:

AM – additive manufacturing;

SLA – stereolithography.

Notations:

D_p, D_{p1} – penetration depth of the uncured photopolymer;

D_{p2} – penetration depth of the cured photopolymer;

E_c – critical energy of the uncured photopolymer;

C_d – cure depth of the photopolymer;

α, β – fitting parameters of the D_{p2} function;

E_{max} – laser exposure on the surface of the photopolymer;

I – irradiance;

I_0 – peak irradiance;

r – radius from the laser beam center;

W_0 – Gaussian half-width;

P_L – power of the laser;

V_s – velocity of the laser;

E – light exposure;

A_0 – absorbed energy proportion.

Introduction

Additive manufacturing (AM) is a fabrication approach in which an object is designed using computer aided design software and produced layer-by-layer through processes such as material extrusion, vat photopolymerization, and powder bed fusion. Initially developed for rapid prototyping and molding, AM has become increasingly accessible in recent years. Advances in materials, hardware, and process control have enabled its adoption for end-use part production across a wide range industries, including the medical field and aerospace engineering.

In the context of vat photopolymerization, stereolithography (SLA) is a high-resolution and high-throughput AM technique that selectively cures liquid photopolymer using a focused laser beam. The curing process involves a combination of optical, thermal, and chemical mechanisms, making SLA modeling an interdisciplinary challenge that requires knowledge in physics, chemistry, and applied mathematics. In practice, physics and chemistry-based models are often preferred due to their interpretability and reliance on material parameters. However, experimental data indicates that the relationship between laser exposure and cure depth can deviate from the linear behavior predicted by classical models, particularly at higher exposures.

The aim of the thesis is to develop a mathematical model that combines physical processes and real experimental data to accurately predict the cure depth of the photopolymer under different exposure conditions.

The objectives of this project are as follows:

- Extend the Jacobs model to include the optical bleaching phenomenon.
- Develop a two-stage function fitting algorithm that optimizes linear and nonlinear parts of the function separately.
- Verify the validity of the extended model under different assumptions by comparing it with the original model.
- Optimize the parameters of the extended model using experimental data and compare its accuracy with a baseline.
- Evaluate the consistency of the extended model.

1. Literature review

1.1. Additive manufacturing

Additive manufacturing (AM), often referred to as 3D printing, comprises a class of fabrication processes in which three-dimensional objects are manufactured layer-by-layer from digital models [1]. In a typical workflow, the object is modeled using computer aided design (CAD) software, which is converted into a stack of thin layers by slicing software before the object is printed. These layers are interpreted as sequential deposition or curing instructions by the AM system [2]. This workflow has many advantages. including:

- Minimized additional tooling – which can significantly reduce the manufacturing cost and time [3].
- Geometric freedom – AM can produce parts with complex geometries [2].
- Reduced material waste – the parts are directly printed into desired shapes, rather than subtracted from a larger component [4].
- Adaptability – the product design can be readily changed [5].

Although AM has historically been applied mainly to prototyping, molding, and simple component fabrication due to limiting factors such as build volume, material limitations, and production time [4], its use has recently expanded toward end-use product manufacturing [5, 6]. Today, AM is also employed for applications such as jigs and fixtures, medical implants, non-load bearing parts in aerospace industries, and more [6].

There is a wide variety of AM approaches, including material extrusion, where melted thermoplastics are deposited through a nozzle; vat photopolymerization, which uses light to cure liquid resins; and powder bed fusion, where lasers or electron beams fuse powdered materials [7]. While each approach offers distinct advantages, this thesis focuses on stereolithography (SLA), a vat photopolymerization technique known for its high resolution, relatively high build speed, and cost effectiveness compared to other high-precision AM processes [7, 8].

1.2. Stereolithography

SLA is an AM process in which a liquid photopolymer resin is selectively exposed to a laser beam that induces curing and forms solid layers [9]. A typical SLA system, pioneered by C. W. Hull, is shown in Fig. 1. In this configuration, the laser is directed along the x and y axes to trace the cross-section of each layer, and once the layer is cured, the stage moves in the z direction to enable layer-by-layer fabrication of the object [10].

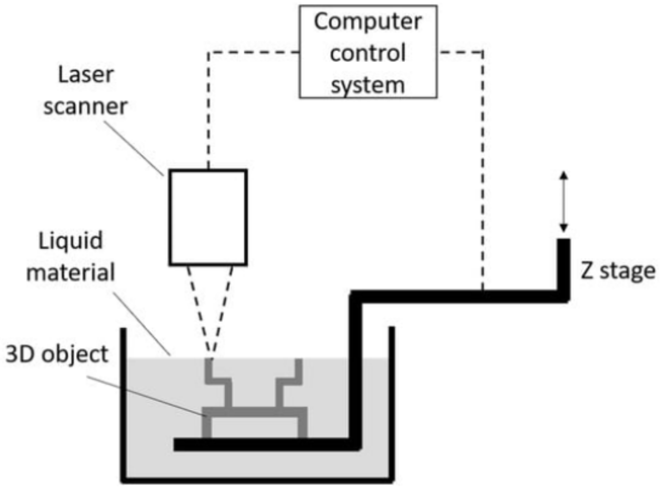

Fig. 1. Hull's stereolithography system [11]

The solidification of the liquid occurs through a process called photopolymerization. When certain materials are exposed to radiation of ultraviolet or visible light, they undergo photochemical reactions that significantly alter their mechanical and chemical properties [12]. Such materials are referred to as photopolymers. A wide range of photopolymers exists; for SLA applications, epoxy and acrylate-based resins are most commonly used, though other materials have been explored [9].

Like other AM techniques, SLA is widely used for prototyping. However, SLA systems are also capable of producing parts with high dimensional accuracy and biocompatible materials, which enables their application in the medical field [13]. One prominent application is dentistry, where implants must be customized for each patient to ensure proper fit and stable bonding between the implant and bone. SLA allows the direct fabrication of patient-specific geometries derived from CT or MRI scan data, enabling accurate representation of complex anatomical shapes [14]. Drug delivery systems manufactured using SLA have also been investigated. Fig. 2 shows five SLA printed implants designed for drug delivery to the ear. Although the results are preliminary, the study demonstrated that the implants successfully absorbed the drug and released it into the ear over extended period without causing adverse health effects [15]. These results further highlight the potential of SLA for applications in personalized medicine.

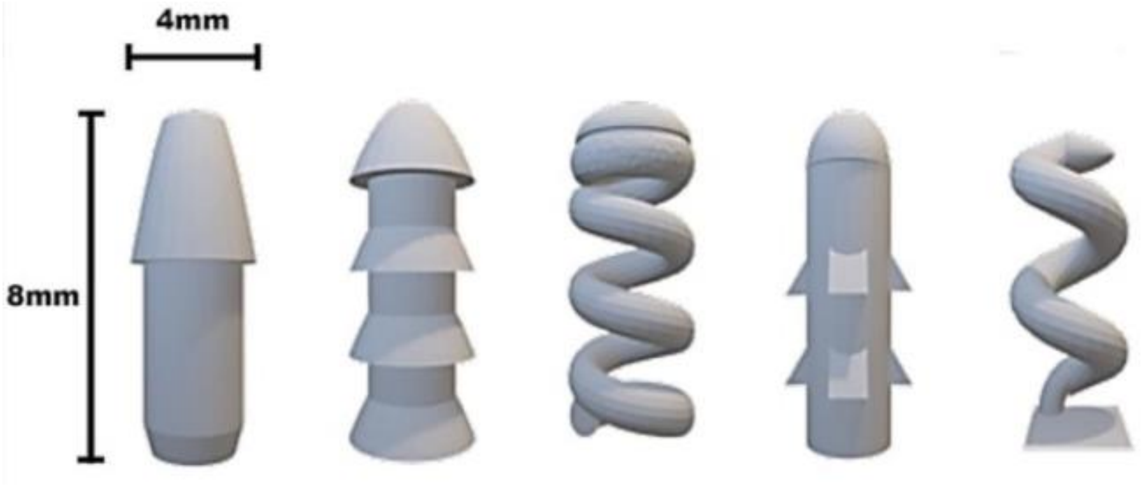

Fig. 2. Drug delivery implants produced using SLA [15]

The fabrication of three-dimensional objects using SLA is a highly precise and exposure-dependent process; therefore, understanding and predicting the behavior of photopolymers under light irradiation is essential. Although SLA is commonly modeled through physical mechanisms such as optical absorption and curing depth prediction [16], several approaches also consider chemical processes occurring within the photopolymer [17, 18], and some integrate both physical and chemical phenomena into a unified description [19].

1.2.1. Physical processes

Physical modeling of SLA focuses on the interaction of the irradiating laser light and the optical properties of the photopolymer. The model introduced by Jacobs is based on three main assumptions: the photopolymer cures once exposed to sufficient amount of energy, the Beer-Lambert law applies to light absorption, and the laser beam has a Gaussian spatial distribution [20].

From the first assumption, a material property called critical energy E_c is defined. E_c represents the minimum required energy for the photopolymer to cure and is typically expressed in mJ/cm^2 [21]. To determine how much material is cured after light exposure, it is necessary to compute how much light energy is absorbed as the beam propagates through the resin.

According to the Beer-Lambert law, as light travels through a medium, the transmitted irradiance decays exponentially [22]:

$$I = I_0 e^{-\mu_a z}, \tag{1}$$

where I_0 is the incident irradiance, z is the depth traveled, and μ_a is the absorption coefficient. This expression can also be rewritten as:

$$I(z) = I_0 e^{-\frac{z}{D_p}}, \tag{2}$$

where D_p is penetration depth which describes the depth at which the irradiance decays to $\frac{1}{e}$ of its surface value. This relationship allows evaluating absorbed energy at any depth.

However, as shown in Fig. 3, a laser beam is not uniform. Its intensity varies radially, and because the beam moves across the resin surface during the exposure, the absorbed energy at a given point accumulates over time. The radial irradiance distribution of an ideal Gaussian beam is given by [23]:

$$I(r) = I_0 e^{-\frac{2r^2}{W_0^2}}. \tag{3}$$

Here, r is the radial distance and W_0 is Gaussian half-width, representing the radius at which the irradiance drops to $\frac{1}{e}$ of the peak value. Combining Beer-Lambert decay in depth (Equation 2) and Gaussian beam radial distribution (Equation 3) enables estimating irradiance at any point in three-dimensional space.

Although real-life lasers do not perfectly follow these assumptions, these relationships sufficiently approximate real exposure conditions in most SLA systems. Since irradiance is instantaneous, additional steps are required to relate it to deposited energy. This will be described further in Section 2.1.

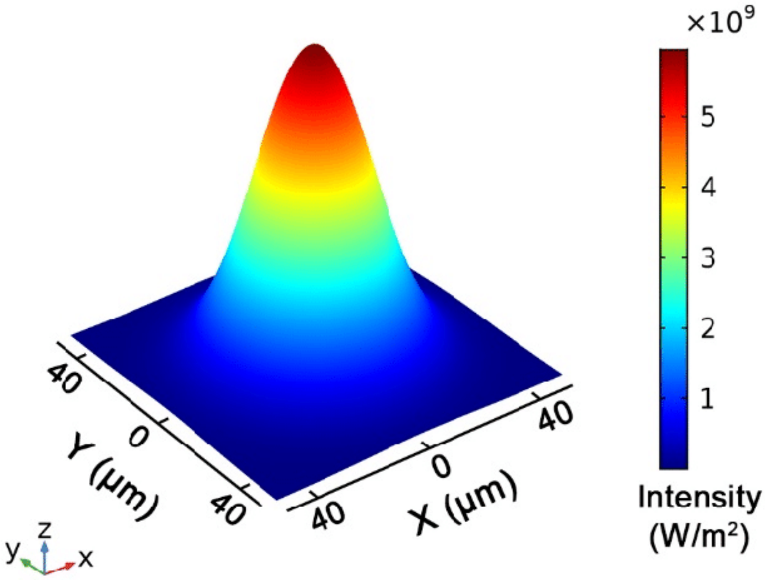

Fig. 3. Irradiance intensity profile of a Gaussian laser beam [24]

In a typical SLA setting, the photopolymers are exposed to energies ranging from 10 mJ/cm^2 to 300 mJ/cm^2, and the lasers operate in the power ranges of 2.5-5.0 mW/cm^2 [25]. In these conditions, the photopolymer properties E_c and D_p are constant, from which it would be reasonable to assume that these are intrinsic material properties. However, experiments conducted by Rudenko et al. and Billerbeck et al. had shown that when the same material is exposed under different light intensities, the critical energy and penetration depth of the material is not constant and is dependent on the light intensity [21, 26]. The penetration depth and the critical energy dependence on light intensity for resin LuxaPrint is shown in Fig. 4. Although the variations are relatively small, the difference between the experiments is statistically significant, therefore, it can be stated that E_c and D_p are not intrinsic physical properties of the material [26], but rather process-dependent empirical parameters.

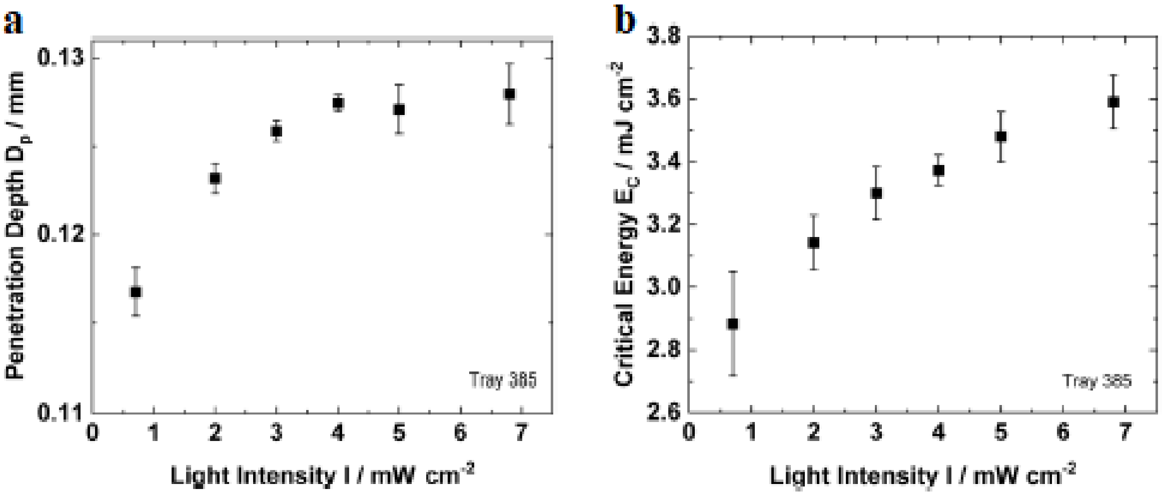

Fig. 4. Resin LuxaPrint Tray a) penetration depth and b) critical energy dependence on light intensity [26]

1.2.2. Chemical processes

The photopolymerization process in SLA is typically described by five components within the system:

- Initiator – a compound that initiates photopolymerization when exposed to light.
- Radicals – highly reactive molecules generated by initiator decomposition.
- Monomers – single, unreacted molecules.
- Polymers – molecular chains formed through monomer reactions.
- Oxygen – which inhibits polymerization by reacting with radicals.

These components interact through three fundamental photopolymerization mechanisms [27]:

1. Initiation – the initiator absorbs light and decomposes to form free radicals, which then react with monomers. Upon bonding with a radical, the monomer becomes highly reactive.
2. Propagation – the activated monomer reacts with additional monomers, forming polymer chains that may continue to react with other monomers or polymer chains.
3. Termination – polymer growth ceases when radicals recombine with other radicals or when polymer chains react with oxygen.

The SLA curing process can therefore be modeled using sets of differential equations that describe the rates of these mechanisms and estimate the evolving concentrations of each component within the system [17, 18].

1.3. Mathematical frameworks of SLA

1.3.1. Jacobs model

One of the methods for characterizing the behavior of SLA systems is by observing the variation of cure depth C_d of the photopolymer with respect to the laser exposure E_{max}. These quantities are related as:

$$C_d = D_p ln \left(\frac{E_{max}}{E_c}\right), \tag{4}$$

where D_p is the penetration depth and E_c is the critical exposure of the photopolymer.

Equation 4, developed by P. F. Jacobs, is known as the working curve equation and forms a fundamental basis of SLA modeling [16]. An experimental example of the working curve is shown in Fig. 5. For clarity, the x axis is set on logarithmic scale, which linearizes the relationship. Both E_{max} and C_d are measured experimentally, allowing D_p and E_c to be estimated: E_c corresponds to the intercept of the fitted line, while D_p corresponds to the slope [28]. Once D_p and E_c are determined, the cure depth for any given laser exposure can be readily calculated using the working cure equation.

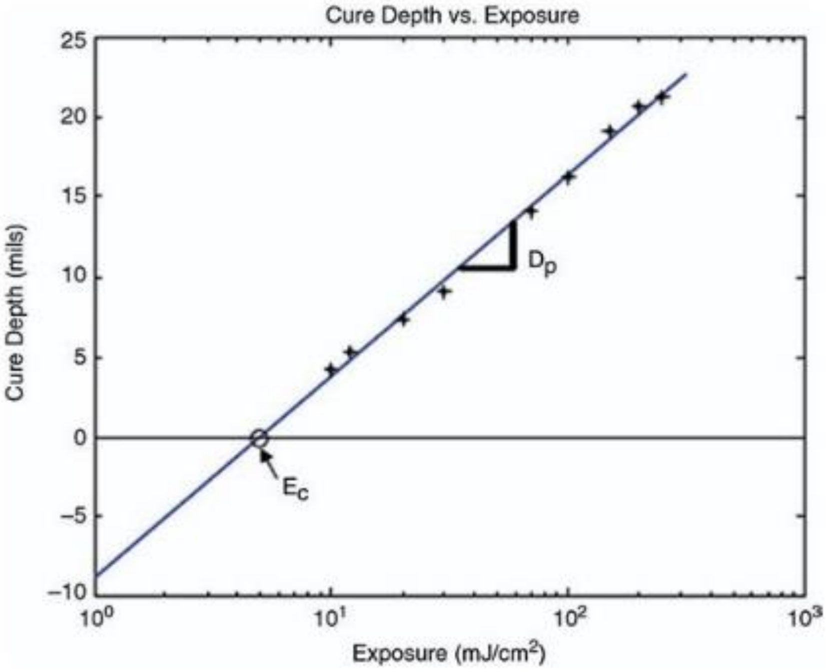

Fig. 5. Experimentally determined working curve [28]

1.3.2. Chemical reaction kinetics model

Another approach to modeling photopolymer curing is based on chemical reaction kinetics. When initiated by light, the reactants undergo a series of chemical processes that lead to the polymerization of the resin. The spatial profile of the cured photopolymer can be estimated from the time-dependent concentrations of these reactants [17]. A model developed by Boddapati and later modified Jariwala et al. employs a set of coupled ordinary differential equations to describe initiation, propagation, and termination mechanisms, thereby determining the concentrations of initiators, radicals, monomers, polymer chains, and oxygen [18]. The mechanisms are defined as [18]:

$$Initiation$$

$$In \rightarrow 2R^*$$

$$R^* + M \overset{k_p}{\rightarrow} P^*$$

$$Propagation$$

$$\mathrm{P}^* + M \overset{k_p}{\rightarrow} P^*$$

$$\mathrm{P}^* + R^* \overset{k_p}{\rightarrow} P^{**}$$

$$\mathrm{P}^* + \mathrm{P}^* \overset{k_p}{\rightarrow} P^{**}$$

$$Termination$$

$$R^* + R^* \overset{k_\mathrm{t}}{\rightarrow} 2R_d$$

$$\mathrm{P}^* + \mathrm{P}^* \overset{k_\mathrm{t}}{\rightarrow} \mathrm{P}_d$$

$$\mathrm{P}^* + R^* \overset{k_\mathrm{t}}{\rightarrow} \mathrm{P}_d$$

$$R^* + O_2 \overset{k_\mathrm{toxy}}{\rightarrow} R_d$$

$$\mathrm{P}^* + O_2 \overset{k_\mathrm{toxy}}{\rightarrow} \mathrm{P}_d$$

where In is initiator, R^* and R_d is radical and dead radical, M is monomer, P and P_d are polymer and dead polymer, k_p, k_t, and k_{toxy} are reaction, termination, and oxidation rates, respectively. These mechanisms are then described by a set of ordinary differential equations [18]:

$$\begin{cases} \dfrac{d[In]}{dt} = -k_d[In] \\ \dfrac{d[R^*]}{dt} = 2k_d[In] - k_p[M][R^*] - 2k_t[P^*][R^*] - 2k_t[R^*]^2 - k_{toxy}[O_2][R^*] \\ \dfrac{d[P^*]}{dt} = k_p[M][R^*] - 2k_t[P^*]^2 - 2k_t[P^*][R^*] - k_{toxy}[O_2][P^*] \\ \dfrac{d[M]}{dt} = -k_p[M][R^*] - k_p[M][P^*] \\ \dfrac{d[P_d]}{dt} = k_t[P^*]^2 + 2k_t[P^*][R^*] + k_{toxy}[O_2][P^*] \\ \dfrac{d[O_2]}{dt} = -k_{toxy}[O_2][R^*] - k_{toxy}[O_2][P^*] - D_{o_2}\left(\dfrac{\partial^2[O_2]}{\partial x^2} + \dfrac{\partial^2[O_2]}{\partial z^2}\right) \end{cases} \tag{5}$$

The equations estimate the concentrations of each reactant. The last equation additionally includes the effect of oxygen diffusion.

Fig. 6 compares the Jacobs model (E_c-D_p model) with the chemical reaction kinetics model simulated in COMSOL. Note that the working curve appears nonlinear because the x axis is plotted on a linear scale. Although the chemical reaction kinetics model agrees better with experimental data at lower exposures, the Jacobs model provides a more accurate overall prediction of the cure height.

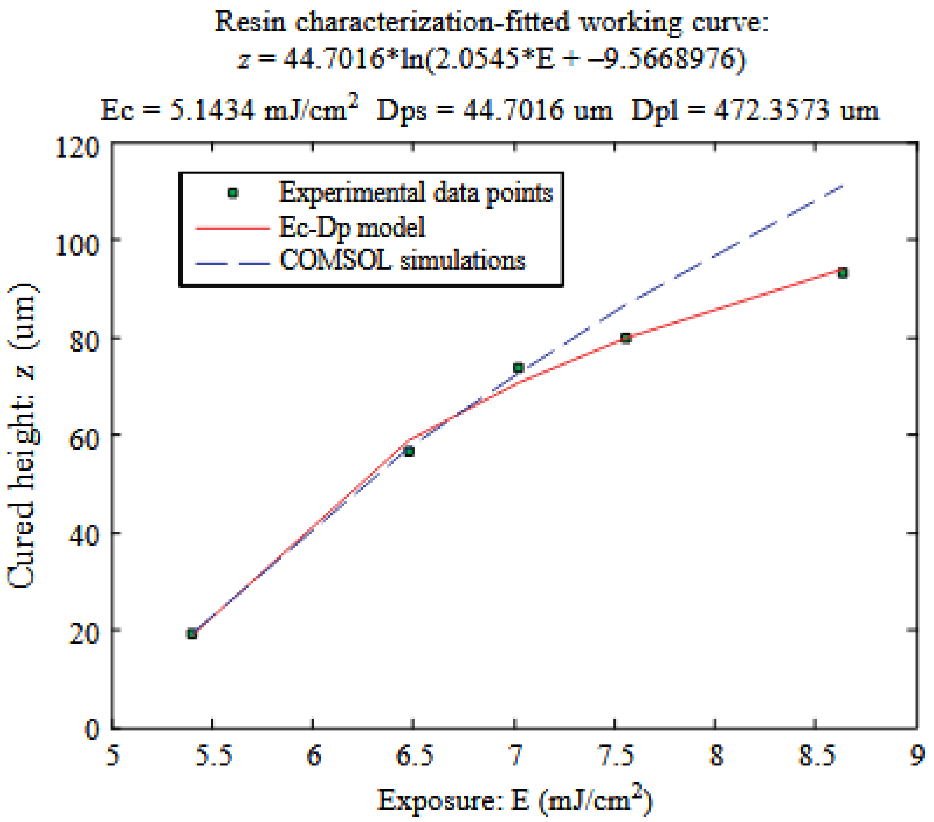

Fig. 6. Estimation of the working curve using Jacobs and chemical reaction kinetics models [18]

However, the Jacobs model has another limitation: it cannot predict the cured shape in mask-based SLA systems. For a Gaussian laser beam, the cured profile follows a parabolic shape that can be described analytically using the Jacobs model (see Chapter 2). In contrast, mask-based SLA employs a digital micromirror device (DMD) and diffuser that generate a flat-top, sharply bounded light pattern, violating the Gaussian assumption. In the model developed by Jariwala et al., the local light intensity serves as a boundary condition; a uniform rectangular profile corresponding to the projected mask was used. Although not explicitly discussed in the paper, the same modeling framework could, in principle, accommodate other illumination patterns, since the photopolymerization kinetics depend only on the local intensity field, rather than the overall beam distribution.

The predicted curing profile from the model is shown in Fig. 7. The simulated shape is consistent with experimental results, though the model slightly overestimates the cured resin width. Furthermore, the model predicts that the width remains constant over time, whereas experiments indicate continued lateral growth. The authors attribute this discrepancy to volumetric shrinkage – the width difference between the experiment and the model is 8-10%, which is consistent with the reported volumetric shrinkage of 12% [18]. Although the model successfully predicts the cured shape of the photopolymer under various illumination conditions, further refinements are required to capture time-dependent lateral growth and to improve height predictions at higher exposures.

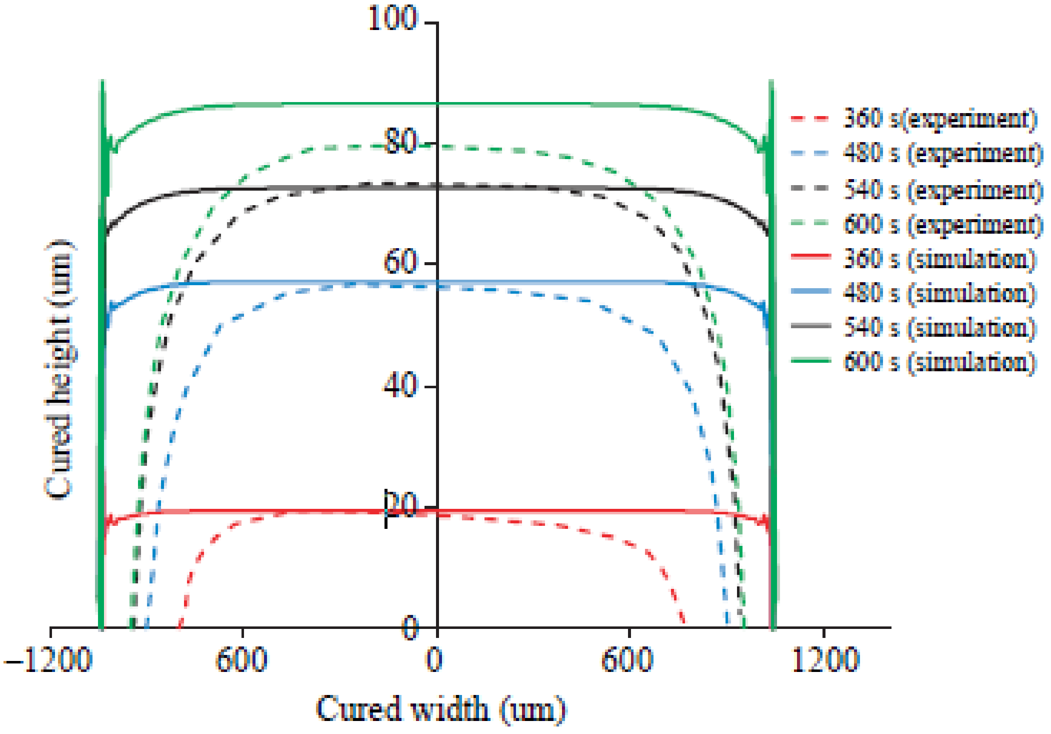

Fig. 7. Curing profile of the experiment and the chemical kinetics model [18]

1.3.3. Hybrid model

A more complex model developed by Blyweert et al. considers light propagation, chemical reaction kinetics, and heat transfer mechanisms to simulate the curing of a multi-component acrylate resin system composed of three different monomers [19]. Light propagation is modeled using Beer-Lamberts law, where the composition of the photopolymer is explicitly considered [19]:

$$\frac{\partial I}{\partial z} = -2.3\epsilon|PI|I. \tag{6}$$

Here, I is the irradiance, ϵ is the molar extinction coefficient of the photopolymer, and $|PI|$ is photoinitiator concentration.

The formulation based on chemical kinetics is similar to the model discussed in Section 1.3.2, although oxygen inhibition effects are neglected. In addition, the model accounts for heat transfer through an energy conservation equation [19]:

$$\rho_M C_{p,M}\frac{\partial T}{\partial t} + \nabla(-\lambda\nabla T) = R_p\Delta \mathrm{H} + \epsilon|PI|I, \tag{7}$$

where ρ_M is the monomer density, $C_{p,M}$ is the monomer heat capacity, T is temperature, λ is the photopolymer thermal conductivity, R_p is the polymerization rate, ΔH is the polymerization enthalpy. This formulation accounts for heat conduction via Fourier's law and photoinitiator absorption, and heat generation due to exothermic nature of polymerization [19]. Since photopolymerization is strongly exothermic, the contribution of laser-induced heating is considered negligible compared to the heat released by the chemical reaction [29].

The model was validated against experimental data, as shown in Fig. 8. Although the simulation slightly overestimated the cure depth, the overall agreement with experiments was good. Cure depth estimation was not the main objective of the study – instead, the model was primarily validated through monomer conversion, polymerization rate, and temperature evolution. Subsequent simulations were used to analyze fundamental stereolithography phenomena, such as influence of photoinitiator concentration, laser scanning speed, light absorption on conversion, heat generation, and polymerization kinetics [19].

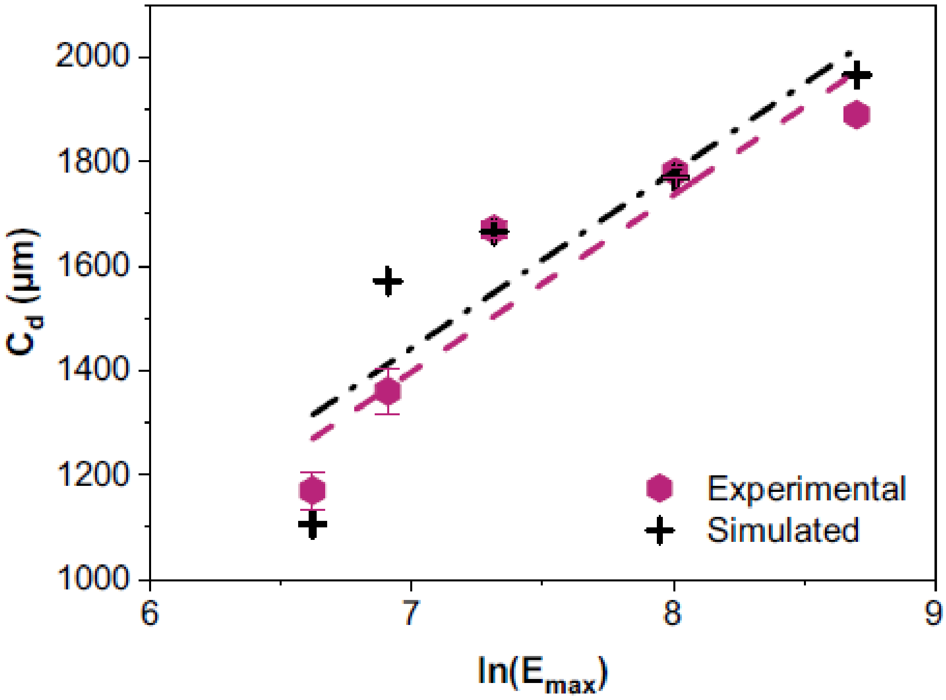

Fig. 8. Estimation of the working curve using the hybrid model [19]

1.4. Nonlinear behavior of the working curve

The working curve equation assumes logarithmic behavior of photopolymer curing, which holds true for lower exposures. However, in certain cases, as shown in Fig. 9, the working curve becomes either super-logarithmic or sub-logarithmic at higher exposures. Jacobs proposed two explanations for the super-logarithmic behavior [16]:

- Optical bleaching – the cured photopolymer exhibits a different absorption coefficient, altering the penetration depth of the medium and thus changing the curvature of the working curve.
- Optical self-focusing – during curing, polymer shrinkage increases the medium density and changes its refractive index, potentially focusing the laser light deeper into the resin and increasing the cure depth at higher exposures.

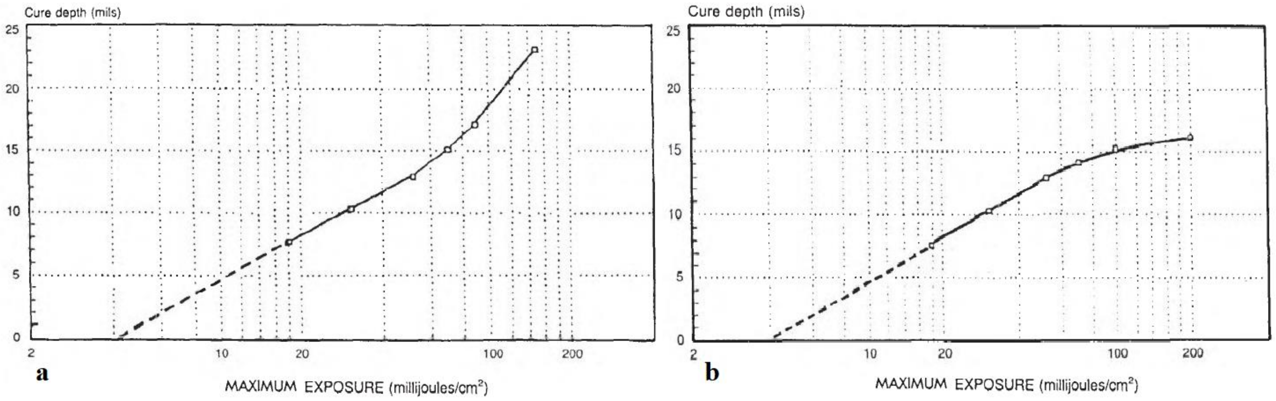

Fig. 9. Working curve with a) super-logarithmic behavior, and b) sub-logarithmic behavior [16]

While several modeling approaches have been developed to predict curing behavior – including chemical reaction kinetics and hybrid models – these frameworks assume constant optical properties and are therefore unable to capture deviations from logarithmic behavior under high exposure conditions.

1.5. Machine learning in SLA

Machine learning algorithms have been increasingly applied to the optimization of SLA processes. An early study conducted by Lee et al. employed a neural network to analyze and predict the influence of SLA process parameters on part dimensional accuracy [30]. During photopolymerization, the resin undergoes shrinkage and distortion due to chemical and thermal effects [31], which can lead to dimensional inaccuracies in printed parts. At the time of the study, these mechanisms were not fully understood, making machine learning a useful tool for identifying underlying relationships in the data. The neural network was trained on 128 samples using three layer-related input parameters and five dimensional errors outputs [30]. When tested on 12 printed parts, the model predicted dimensional errors with an accuracy of approximately 10 µm. The study also concluded that thinner layers, smaller hatch overcures, and larger hatch spacings improve the part dimensional accuracy [30].

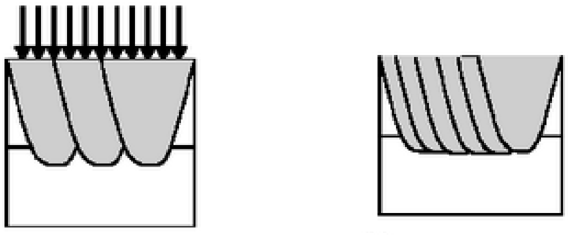

(a) Saturation caused by positive hatch overcure

(b) Saturation caused by positive hatch overcure

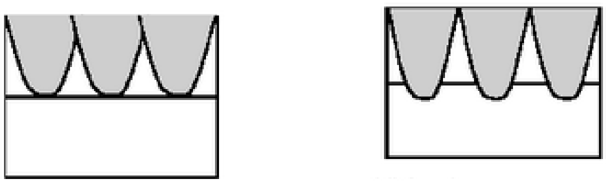

(c) Inadequacy caused by negative hatch overcure

(d) Inadequacy caused by negative hatch overcure

Fig. 10. Hatch overcure visualization [30].

In a related study, laser power, scanning distance, and scanning speed were used as inputs to a neural network to predict process time, dimensional error, and mechanical properties SLA printed parts [32]. The model achieved prediction errors below 3% and was integrated with a multi-objective optimization algorithm that minimized forming error and process time, while maximizing structural strength. The primary goal was to reduce the time required for manual parameter testing. The combined neural network and optimization framework improved average dimensional accuracy and mechanical strength of the printed part by more than 13% [32], highlighting the potential of machine learning for enhancing SLA performance.

Machine learning has also found important applications in SLA-based bioprinting. Due to the scarcity of organs, artificial tissues and organs are increasingly fabricated using techniques such as SLA [33]. A critical challenge in bioprinting is maintaining cell viability, as non-biocompatible printed structures can induce necrosis and apoptosis [34]. Developing physics-based models to predict cell viability is challenging due to the complexity of biological systems; consequently, machine learning approaches have been explored [35]. One study demonstrated that an ensemble model combining ridge regression, k-nearest neighbors, random forest, and neural networks achieved R^2 score of 0.953 when predicting cell viability based on UV intensity, UV exposure time, hydrogel concentration, and layer thickness [35].

Despite these advances, research applying machine learning to cure depth prediction in SLA remains limited. One notable study employed conditional generative adversarial networks (cGANs) to predict the three-dimensional geometry of single-layer prints in digital light processing (DLP) systems [36]. DLP is a form of SLA in which an entire layer is exposed simultaneously using a projected light pattern, rather than by continuous laser scanning [37]. In this approach, 2D greyscale images representing pixel-level light exposure were used to predict voxel-wise cure depth. As shown in Fig. 11, the cGAN successfully captured pixel-to-pixel interactions and accurately predicted complex single-layer geometry, demonstrating that machine learning can be used to predict cure depth in DLP systems. Given the complexity of pixel interactions in DLP, such data-driven modeling is particularly well suited for this application.

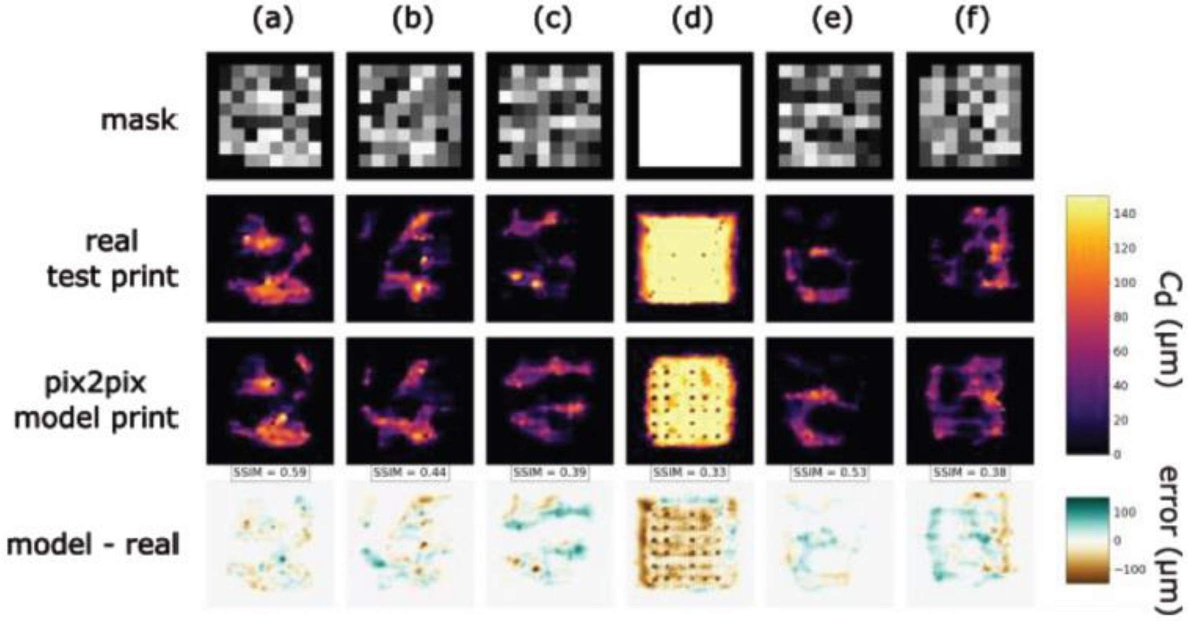

Fig. 11. Printed and simulated part comparison using the same projected light mask [36]

The limited use of machine learning for cure depth prediction in continuous laser scanning SLA may be attributed to the black-box nature of machine learning models. Since cure depth in SLA has been extensively studied using physics-based approaches such as Jacobs model, fully data-driven methods are often avoided, even when physical models fail under certain conditions. In practice, it is often preferable to rely on known physical parameters and operate within regimes where established models remain valid, rather than adopt models lacking physical interpretability. A potential compromise is grey-box modelling, which integrates prior theorical knowledge with data-driven components to account for both the known physical mechanisms and unmodeled effects [38].

1.6. Grey-box models

A white-box model describes a system using known physical laws and parameters, allowing the system behavior to be interpreted directly from its formulation. In contrast, a black-box model has no explicit physical meaning and predicts the outcomes solely based on patterns learned from data. Grey-box models lie between these two extremes: part of the prediction is governed by physically meaningful parameters, while remaining behavior is captured through data-driven components that account for unknown or unmodeled effects [38]. There are several approaches to grey-box modeling. One approach constrains black-box model parameters using physical insight, while another augments a white-box model with additional empirical parameters that are identified from experimental data [39]. The main advantages of grey-box models are improved interpretability compared to black-box models and improved predictive accuracy compared to purely white-box models [39, 40].

One of the major challenges in AM is data scarcity, which can be attributed to several factors related to experimental data collection [41, 42]:

- Data exists in many formats (e.g. STL files, sensor measurements, process parameters), making integration, synchronization, and unified analysis difficult.
- There is a lack of standardized data structures, formats, and APIs for managing and sharing AM data across platforms and machines.
- Existing data collection platforms and graphical user interfaces are often complex and unintuitive for non-expert users.
- The data collection, storage, and management process is costly and time-consuming.

To address data scarcity in AM, Tamir et al. proposed a physics-driven data collection framework that integrates finite element analysis (FEA) with physics-informed machine learning (PIML) [42]. In their approach, FEA simulations encode thermo-mechanical laws governing heat transfer, residual stress, and warpage, forming the white-box component of the model. The simulation-generated data are then used to train data-driven machine learning models that predict part quality metrics, such as deflection and von Mises stress under varying process conditions, which constitutes the black-box component. This hybrid structure reduces reliance on costly experiments while retaining physical consistency [42], which is a key requirement for AM applications. Despite the demonstrated advantages of grey-box modeling approaches, their application within AM remains limited, with relatively little research focusing on hybrid models that explicitly combine physics-based formulations with data-driven techniques.

1.7. Summary of literature review

SLA is AM technique that rapidly produces high dimensional accuracy parts by exposing liquid photopolymer using a precisely focused laser beam. It is widely applied in prototyping, dentistry, medical implant production, and related fields. SLA is characterized by using various mathematical models, the most widely used being the Jacobs model. While the working curve is typically linear at low exposures, experimental data has shown that it can become nonlinear at higher exposures. One proposed mechanism explaining super-logarithmic behavior is optical bleaching, which accounts for the changes in the optical properties of the cured photopolymer.

Currently, no existing model accurately predicts the cure depth of the photopolymer in SLA across super-logarithmic or sub-logarithmic working curve behaviors. Although machine learning techniques have been applied to SLA for process optimization, the cure depth has not been predicted using black-box models, likely due to their lack of physical interpretability. Similarly, grey-box modeling approaches have not been explicitly applied to SLA, despite their demonstrated effectiveness in other AM contexts.

This thesis focuses on the optical bleaching phenomenon as a mechanism for modeling nonlinear working curve behavior. The objective is to extend the Jacobs model by incorporating optical bleaching and use experimental data to optimize additional model parameters, resulting in a grey-box formulation that combines physical modeling with data-driven optimization. While Jacobs attributes optical bleaching primarily to super-logarithmic behavior, changes in the penetration depth may occur in either direction depending on material properties. Therefore, this thesis examines optical bleaching as a potential explanation for both super-logarithmic and sub-logarithmic behaviors. Specifically, an increase in the penetration depth of the cured photopolymer is expected to produce super-logarithmic behavior, whereas a decrease is expected to result in sub-logarithmic behavior.

2. Methods

2.1. Jacobs model

2.1.1. The exposure equation

When a Gaussian laser scans across the surface of a photopolymer at velocity V_s, the highest dose of irradiance I falls into the center of the beam, as shown in Fig. 12. The irradiance drops exponentially in radius r from the center [16]

$$I(r,0) = I_0 e^{\left(\frac{-2r^2}{W_0^2}\right)}, \tag{8}$$

where I_0 is the peak irradiance, W_0 is the Gaussian half-width. I_0 is related to the power of the laser P_L as [16]:

$$I_0 = \frac{P_L}{\pi W_0^2}. \tag{9}$$

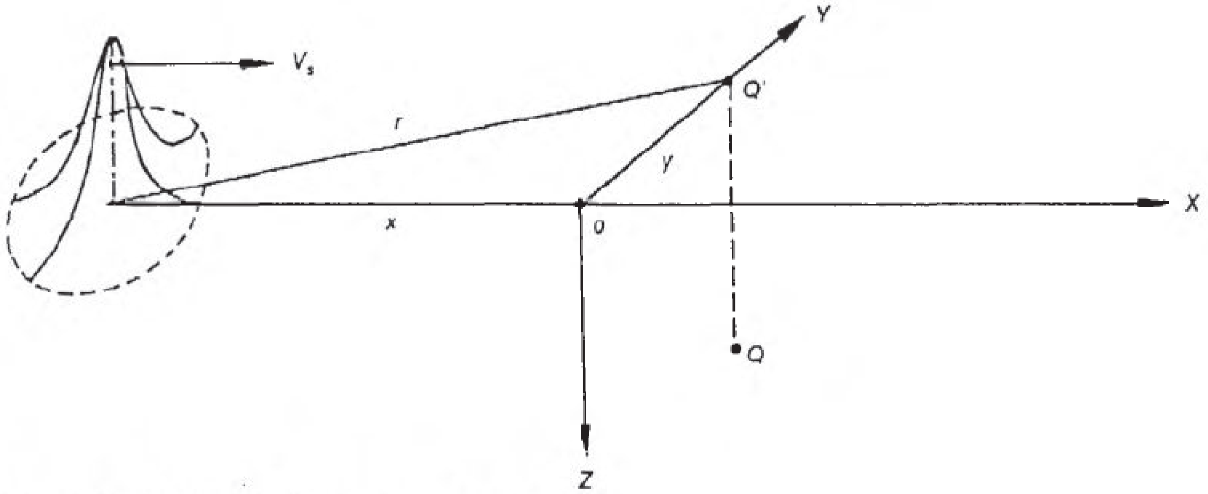

Fig. 12. Gaussian laser beam scan [16]

Measuring irradiance I, however, is impractical, because it is instantaneous power delivered at the surface – as the laser moves, the surface is exposed to different doses of irradiance over time. It is more practical to measure total light exposure on the surface of the photopolymer. Light exposure E on the surface is the integral of the irradiance over time [16]:

$$E(y,0) = \int_{t=\infty}^{-t=\infty} I[r(t),0]\,dt. \tag{10}$$

It was shown by Jacobs that combining Equations 8-10 and utilizing the geometry of the system seen in Fig. 12, the exposure can be expressed as [16]

$$E(y,0) = \frac{2P_L}{\pi W_0^2 V_s} e^{(\frac{-2y^2}{W_0^2})} \int_{-\infty}^{\infty} e^{(\frac{-2x^2}{W_0^2})} dx. \tag{11}$$

The integral is symmetrical, therefore Equation 11 can be rewritten as

$$E(y,0) = \frac{4P_L}{\pi W_0^2 V_s} e^{(\frac{-2y^2}{W_0^2})} \int_{0}^{\infty} e^{(\frac{-2x^2}{W_0^2})} dx. \tag{12}$$

Substituting $\frac{2x^2}{W_0^2}$ with dimensionless variable v^2, the integral can be solved, and the final expression of exposure on the surface of the resin becomes [16]

$$E(y,0) = \sqrt{\frac{2}{\pi}} \frac{P_L}{W_0 V_s} e^{(\frac{-2y^2}{W_0^2})}. \tag{13}$$

Additionally, the exposure can also be calculated at any depth z of the photopolymer by including absorption function:

$$E(y,z) = \sqrt{\frac{2}{\pi}} \frac{P_L}{W_0 V_s} e^{(\frac{-2y^2}{W_0^2})} e^{(\frac{-z}{D_p})}. \tag{14}$$

2.1.2. The working curve equation

Photopolymer cures when it is exposed to critical energy E_c. If the laser moves at a constant velocity along x axis with constant power, the photopolymer is cured into a parabolic shape, as shown in Fig. 13. In this example, the cured part of the photopolymer had been exposed to $E > E_c$, while the uncured part received $E < E_c$. The boundary between the cured and uncured part is where the light exposure is exactly $E = E_c$ – the photopolymer transitions from liquid to solid phase, which is called the gel point [16].

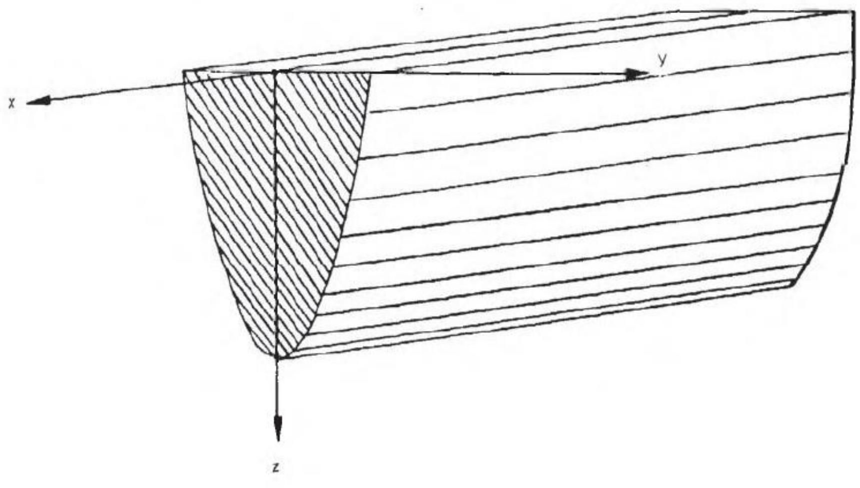

Fig. 13. Schematic view of a cured line [16]

Equation 14 can be rewritten for these gel points y^* and z^* to find the critical exposure

$$E(y^*, z^*) = E_c = \sqrt{\frac{2}{\pi}}\frac{P_L}{W_0 V_s} e^{(\frac{-2y^{*2}}{W_0^2})} e^{(\frac{-z^*}{D_p})}. \tag{15}$$

Note that for this function, any combination of y* and z* works, as long as it is on the boundary of the cured photopolymer. Equation 15 is rearranged using simple algebra and logarithm properties to move the variables to the left-hand side of the equation [16]:

$$\frac{2y^{*2}}{W_0^2} + \frac{z^*}{D_p} = ln\left(\sqrt{\frac{2}{\pi}}\frac{P_L}{W_0 V_s E_c}\right). \tag{16}$$

Equation 16 describes the boundary of the cured photopolymer. In practice, the most important part of the curve is the center, which coincides with the laser center – this is the maximum cure depth C_d of the photopolymer. Substituting $y^* = 0$ and $z^* = C_d$, Equation 16 becomes

$$\frac{C_d}{D_p} = ln\,(\sqrt{\frac{2}{\pi}}\frac{P_L}{W_0 V_s E_c}), \tag{17}$$

which can be further simplified by including the centerline laser exposure E_{max}

$$E(0,0) = E_{max} = \sqrt{\frac{2}{\pi}}\frac{P_L}{W_0 V_s}, \tag{18}$$

and combining Equations 17 and 18, the cure depth C_d becomes

$$C_d = D_p ln\,(\frac{E_{max}}{E_c}), \tag{19}$$

which is the **working curve equation**.

2.2. Modified Jacobs equation

2.2.1. Zone of influence

Equation 12 assumes that the laser scan path is infinite, and although it seems impractical, majority of the laser energy is received from a relatively short laser scan range, which is why the model works in practice. However, to implement the optical bleaching phenomena, the laser scan needs to be divided into two or more steps, therefore, selecting infinite scan path is no longer viable. For that, a zone of influence is selected – a laser scan region, where majority of the energy is accounted for. Jacobs defined that on any point of the resin surface, 99.99% of the energy is received from the laser scan region that spans 2.15 W_0 to both sides from the point [16]. In this case, Equation 12 becomes

$$E(y,0) = \frac{4P_L}{\pi W_0^2 V_s} e^{\left(\frac{-2y^2}{W_0^2}\right)} \int_0^{2.15W_0} e^{\left(\frac{-2x^2}{W_0^2}\right)} dx. \tag{20}$$

The integral is solved using the same substitution

$$\mathrm{v}^2 = \frac{2x^2}{W_0^2}, \tag{21}$$

$$\mathrm{v} = \left(\frac{\sqrt{2}}{W_0}\right) x, \tag{22}$$

$$dv = \left(\frac{\sqrt{2}}{W_0}\right) dx, \tag{23}$$

$$dx = \left(\frac{W_0}{\sqrt{2}}\right) dv. \tag{24}$$

The integral limits:

$$x = 0, \mathrm{v} = 0 \tag{25}$$

$$x = 2.15W_0, \mathrm{v} = \left(\frac{\sqrt{2}}{W_0}\right) * 2.15W_0 \approx 3.04. \tag{26}$$

With the substitutions and recomputed integral limits, the following equation is obtained:

$$E(y,0) = \frac{2\sqrt{2}}{\pi} \frac{P_L}{W_0 V_s} e^{\left(\frac{-2y^2}{W_0^2}\right)} \int_0^{3.04} e^{(-\mathrm{v}^2)} d\mathrm{v}. \tag{27}$$

The upper integral limit is what defines the scan range (or time, as it is proportional). For example, for 50% of the scan time, the upper bound is set as 1.52.

Solving the integral results in the following equation:

$$E(y,0) = \frac{0.88621 * 2\sqrt{2}}{\pi} \frac{P_L}{W_0 V_s} e^{\left(\frac{-2y^2}{W_0^2}\right)}. \tag{28}$$

And including the absorption function, the full equation becomes

$$E(y,z) = \frac{0.88621 * 2\sqrt{2}}{\pi} \frac{P_L}{W_0 V_s} e^{\left(\frac{-2y^2}{W_0^2}\right)} e^{\left(\frac{-z}{D_p}\right)} = \frac{2\sqrt{2}A_0}{\pi} \frac{P_L}{W_0 V_s} e^{\left(\frac{-2y^2}{W_0^2}\right)} e^{\left(\frac{-z}{D_p}\right)}. \tag{29}$$

The coefficient A_0 represents the absorbed energy proportion, which is not proportional to the scan time due to the exponential decline in the integral. The validity of Equation 29 can be confirmed by comparing its first term with the first term of Equation 14, as the rest of the equation is the same

$$\sqrt{\frac{2}{\pi}} \approx 0.79788, \ \frac{0.88621*2\sqrt{2}}{\pi} \approx \ 0.79787,$$

therefore:

$$\frac{0.88621*2\sqrt{2}}{\pi}\frac{P_L}{W_0V_s}e^{\left(\frac{-2y^2}{W_0^2}\right)}e^{\left(\frac{-z}{D_p}\right)} \approx \sqrt{\frac{2}{\pi}}\frac{P_L}{W_0V_s}e^{\left(\frac{-2y^2}{W_0^2}\right)}e^{\left(\frac{-z}{D_p}\right)}.$$

Which confirms that selecting an appropriate zone of influence is almost equivalent to selecting infinite laser scan range.

2.2.2. Two-step scanning process

Implementation of optical bleaching phenomena requires at least two steps:

1) The laser light is absorbed by the liquid photopolymer, that causes it to cure in a parabolic shape. This step is identical to the regular SLA process, however, here the assumption is that the surface was scanned only partially.
2) The laser light first penetrates the cured photopolymer, and then reaches the liquid photopolymer, where the same process as in the first step occurs. In this case, some of the energy is absorbed by the cured resin. The penetration depth of the cured resin is different from the liquid resin, which can cause either more or less light to pass through it. In this step, the scan time is the leftover time from the first step.

These two steps are visualized in Fig. 14, where in this case, the partial scan is 20% of the full scan time. In the first step, the laser light cures the area indicated by the partial scan, and in the second step, the laser light penetrates the cured area of the partial scan, then cures the rest of the area.

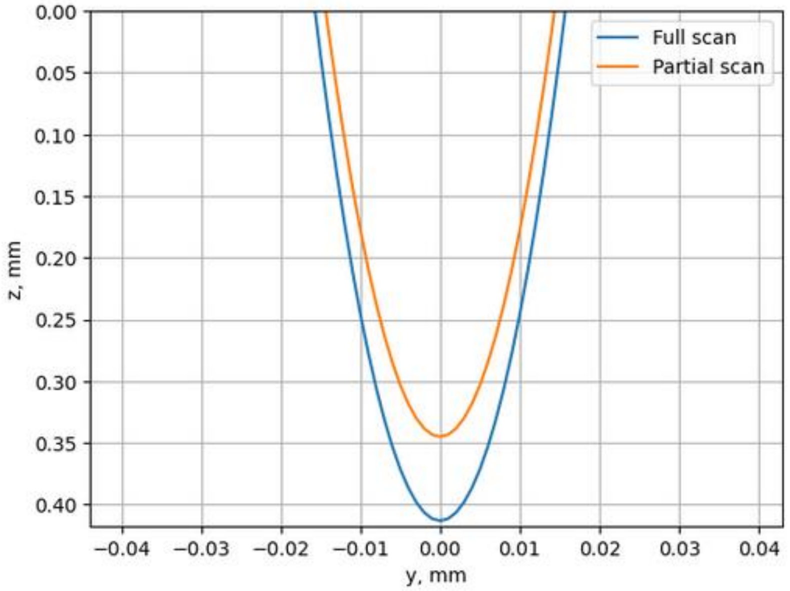

Fig. 14. Cured resin profile in partial and full scan

To apply this idea to the working curve equation, it is split into two parts. For the two-step scanning process, the energy must be divided into steps, and the change in penetration depth D_p needs to be implemented. This is done by modifying Equation 29 and inserting it into Equation 19. The first step is similar to the original model:

$$E(0,0) = E_1 = \frac{2\sqrt{2}A_1}{\pi}\frac{P_L}{W_0V_s}, 0 < A_1 < A_0 \tag{30}$$

$$C_{d1} = D_{p1} ln\left(\frac{E_1}{E_c}\right). \tag{31}$$

Here A_1 is a part of the absorbed energy proportion, corresponding to partial scan time, and D_{p1} is the penetration depth of the uncured photopolymer. The second step is different:

$$E(0, C_{d1}) = E_2 = \frac{2\sqrt{2}A_2}{\pi}\frac{P_L}{W_0V_s}e^{\left(\frac{-C_{d1}}{D_{p2}}\right)}, A_2 = A_0 - A_1 \tag{32}$$

$$C_{d2} = D_{p1} ln\left(\frac{E_2+E_c}{E_c}\right)(20). \tag{33}$$

Equation 32 corresponds to the remaining energy E_2 that reaches the interface between the two materials. It uses different coefficient A_2 that correspond to the remaining scan time. Additionally, the absorption term $e^{\left(\frac{-C_{d1}}{D_{p2}}\right)}$ is included, which accounts for the energy lost in cured photopolymer with the penetration depth of D_{p2} at the cured depth C_{d1}. The cure depth C_{d2} is then calculated using this remaining energy E_2 for the same uncured photopolymer with the penetration depth of D_{p1}. Additionally, during the first step, the interface has already been exposed to the critical energy E_c, therefore the total delivered energy at the second step is equal to $E_2 + E_c$, which is included in the calculation of the cure depth C_{d2}.

Finally, the total cure depth is then equal to:

$$C_d = C_{d1} + C_{d2}. \tag{34}$$

For plotting purposes, the maximum exposure is calculated separately using the same equation as the original model, as the total exposure remains the same regardless of how many steps the process was split into:

$$E_{max} = \frac{2\sqrt{2}A_0}{\pi}\frac{P_L}{W_0V_s}. \tag{35}$$

Equation 35 is almost identical to Equation 18, but this expression was used for the sake of consistency. Note that the aforementioned derivation is entirely **one of the results of this thesis**.

2.2.3. Multi-step scanning process

Multi-step scanning process can be implemented analogously as the two-step case: the first step remains unchanged, while the second step is repeated n times. However, this approach introduces a limitation. If the absorbed energy proportion coefficient A_0 is divided by n, the resulting time steps are not uniform, because the absorbed energy is not linearly proportional to time.

To obtain equal time steps, Equation 27 is modified to include the absorption term, and the upper integration limit is replaced with a constant $t_0 = 3.04$:

$$E(y,z) = \frac{2\sqrt{2}}{\pi}\frac{P_L}{W_0 V_s} e^{\left(\frac{-2y^2}{W_0^2}\right)} e^{\left(\frac{-z}{D_p}\right)} \int_0^{t_0} e^{(-v^2)}\, dv. \tag{36}$$

This formulation allows the exposure to be divided into equal time steps. The parameter t_0 is dimensionless and proportional to both scan time and distance.

The first step in the multi-step process is

$$E(0,0) = E_0 = \frac{2\sqrt{2}}{\pi}\frac{P_L}{W_0 V_s} \int_0^{\frac{t_0}{n}} e^{(-v^2)}\, dv \tag{37}$$

$$C_d = D_{p1} ln\left(\frac{E_0}{E_c}\right). \tag{38}$$

At step i the equations become

$$E(0,C_d) = E_i = \frac{2\sqrt{2}}{\pi}\frac{P_L}{W_0 V_s} e^{\left(\frac{-C_d}{D_{p2}}\right)} \int_{\frac{t_0}{n}*i}^{\frac{t_0}{n}*(i+1)} e^{(-v^2)}\, dv \tag{39}$$

$$C_{di} = D_{p1} ln\left(\frac{E_i + E_c}{E_c}\right) \tag{40}$$

$$C_d = C_d + C_{di}. \tag{41}$$

This procedure is repeated $n - 1$ times. The process is visualized in Fig. 15, where the largest increases in cure depth occur during the initial steps, consistent with the exponential decay of the integral. Again, this derivation is **one of the key results of the thesis** and will be referred to as the **full model**.

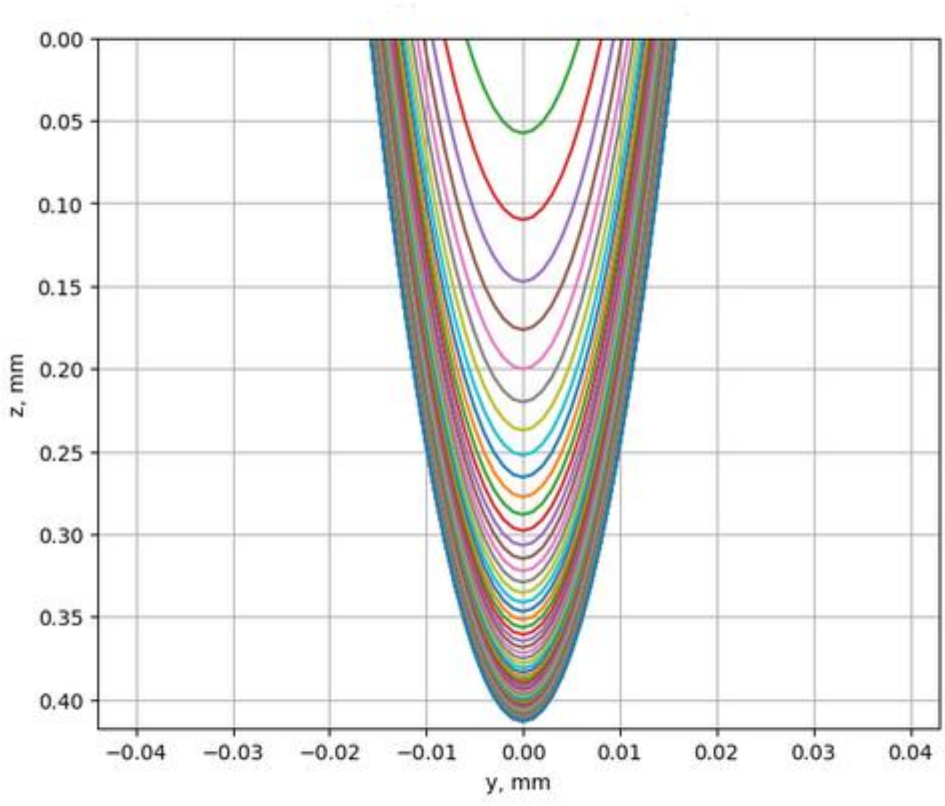

Fig. 15. Resin curing process with equal time steps

2.2.4. Simplified model

The model derived in the previous subsection assumes that the laser scans along the x axis, which is typical during SLA operation. In experimental testing, however, the laser is often stationary and only the exposure time is varied.

Under this assumption, Equation 36 simplifies to

$$E(y,z) = It\, e^{\left(\frac{-2y^2}{W_0^2}\right)} e^{\left(\frac{-z}{D_p}\right)}, \tag{42}$$

where I is the laser intensity and t is the exposure time. The expression for C_d remains unchanged. Time steps and the parameter D_{p2} can also be incorporated into this simplified model. The first step becomes

$$E(0,0) = E_0 = I\Delta t\ (30) \tag{43}$$

$$C_d = D_{p1} ln\, (\frac{E_0}{E_c}). \tag{44}$$

At step i,

$$E(0, C_d) = E_i = I\Delta t\, e^{\left(\frac{-C_d}{D_{p2}}\right)} \tag{45}$$

$$C_{di} = D_{p1} ln\, (\frac{E_i + E_c}{E_c}) \tag{46}$$

$$C_d = C_d + C_{di}. \tag{47}$$

Although Equation 42 explicitly includes time, Equation 36 can still be applied to the simplified case. Comparing Equations 36 and 42 shows that the governing parameters are proportional:

$$\frac{P_L}{W_0 V_s} \sim \text{It}.$$

From a mathematical standpoint, it is therefore valid to vary an alternative parameter – such as P_l – to represent changes in exposure time, even when the laser power is constant in the experiment.

Equation 39 includes timesteps within the integral, whereas Equation 45 does not. A Numerical comparison (see Section 3.1.4) shows that this difference results in a 2% deviation in predicted cure depth. Because the focus of this thesis is on the mathematical behavior of the model rather than on enforcing a specific exposure mechanism, the full model is used in all cases.

2.3. Datasets

The datasets used in this thesis consist of experimentally measured cure thicknesses as a function of laser exposure, collected from several SLA experiments. The model was evaluated using two datasets:

- WCM dataset – provided by the company AmeraLabs, which specializes in photopolymer resin production for 3D printing. It contains 30 experiments that show relatively strong consistency.
- NIST dataset – a publicly available dataset from a study on the working curve behavior in vat photopolymerization [43]. It includes 35 experiments that exhibit substantial variability between measurements.

2.3.1. WCM dataset

WCM experiments are shown in Fig. 16. Most of the data is relatively linear, but for some cases, the linearity is lost on higher laser exposure. Each experiment also contains some zero data, which was excluded from the model for accuracy purposes.

This dataset was mostly used to check the model consistency – the experiments were performed on resins with similar properties; therefore, the model parameters should also be consistent for similar data.

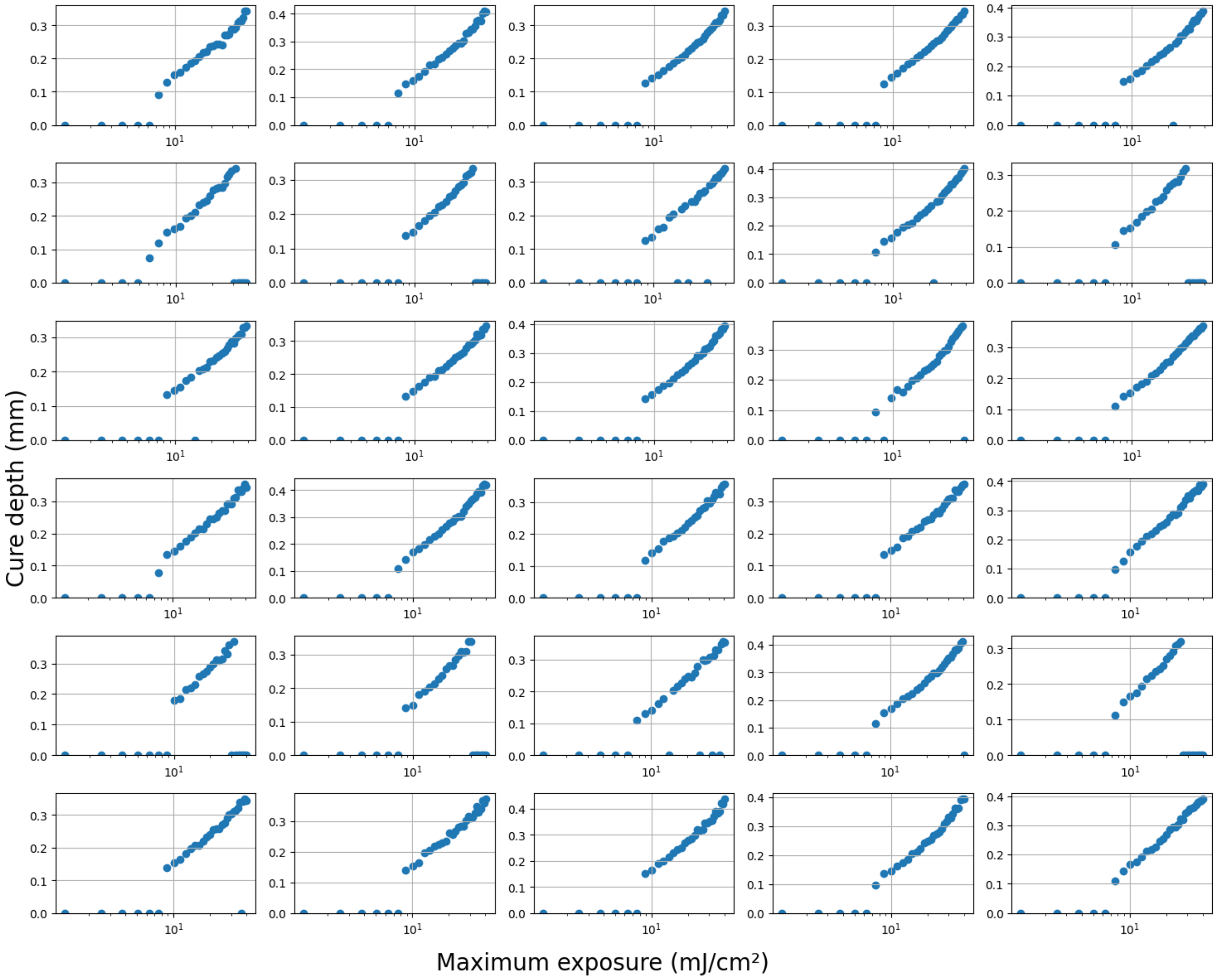

Fig. 16. WCM dataset for measured cure thickness as a function of laser exposure

2.3.2. NIST dataset

NIST experiments are shown in Fig. 17. The data is varied – some experiments resulted in linear data, while others had shown very pronounced curves at higher exposure in either direction, which is useful for model testing under various conditions.

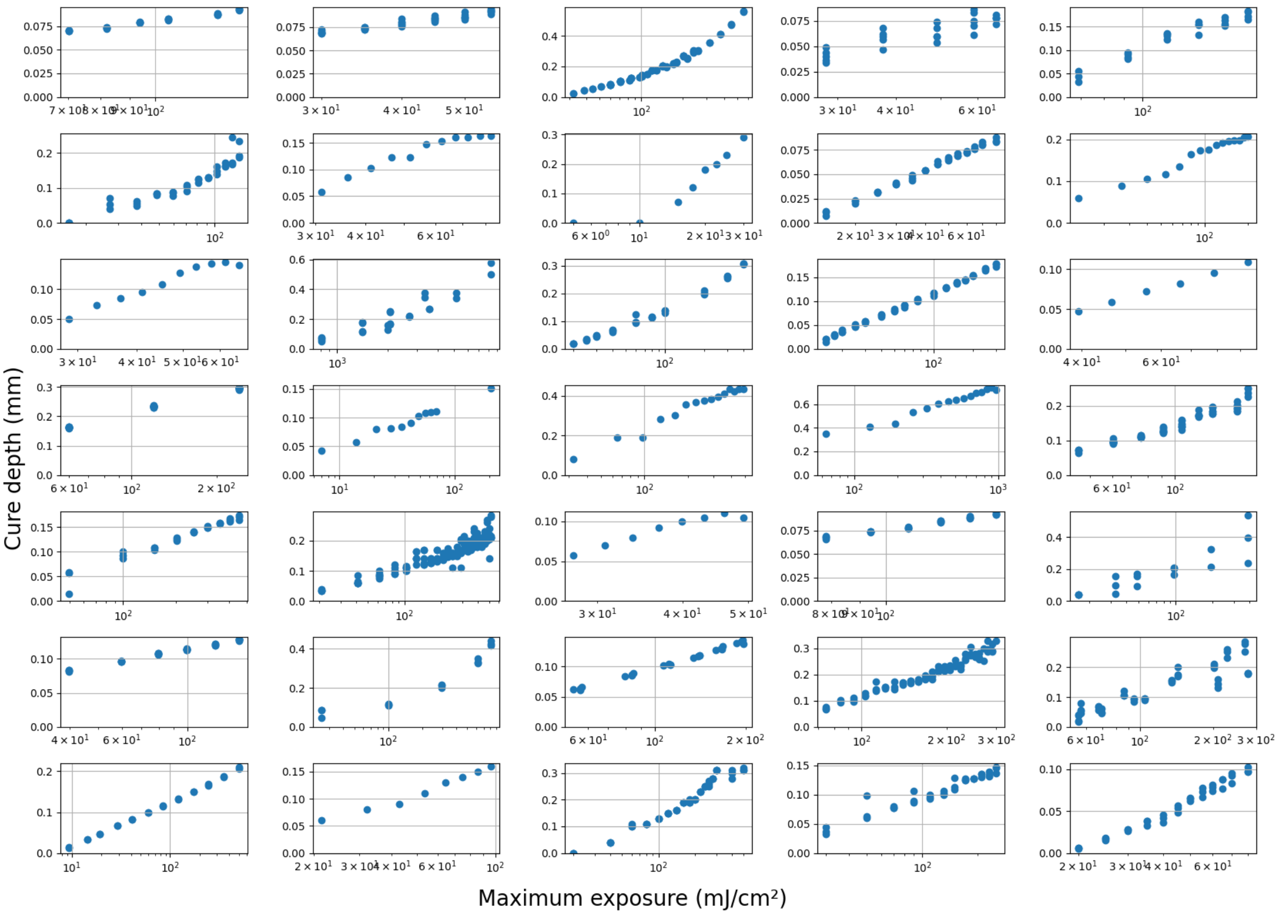

Fig. 17. NIST dataset for measured cure thickness as a function of laser exposure

2.4. Two-stage function fitting

The model parameters W_0,V_s,t_0, and n are constant, while the parameter P_l is used to define the range of the working curve. The parameters D_{p1}, and E_c are typically determined experimentally by obtaining the slope and the intercept of the linear portion of the data. To account for nonlinearity, the model also uses D_{p2}, which will be shown in Section 3.1.3 to change dynamically according to the parameters α and β. Manually selecting these parameters may be sufficient for a single experiment, but since the model will be tested for 75 different experiments, manual selection is not practical. Therefore, a two-stage function fitting procedure is performed for these datasets.

In the first stage, a linear regression model is fit to the linear portion of the experimental data to determine D_{p1}, and E_c. The linear portion is identified by initially selecting a certain number of points and masking them as "linear". A linear regression model is fit for these datapoints, and two subsequent points are then checked against the linear model: if both points fall outside a predefined tolerance, the procedure is stopped; otherwise, the first of the two points is added to the linear set, and the next two points are evaluated. This approach of checking two points accounts for local deviations in the data. Once all linear points are identified, a final linear regression is performed to obtain D_{p1}, and E_c.

In the second stage, the model uses the fixed values of D_{p1}, and E_c obtained from the first stage, while PySwarms algorithm is employed to optimize the α and β parameters. This algorithm uses a population of particles that explore the parameter space by randomly selecting values within a defined range and evaluating model's accuracy. The procedure is repeated over a predefined number of iterations to converge on the best fitting α and β parameters. After testing, the parameter space for α was set to $(-1 * 10^{-6} \ldots 1 * 10^{-6})$, and for β it was set to $(1 \ldots 5)$.

2.5. Schematic of the model development

To summarize, in the first stage of model development, a constant $A_0 = 0.88621$ is introduced, which represents 99.99% effective scan range, but D_p remains unchanged. In the second stage, the model is split into two steps – the first step is similar to the previous stage, but on the second step, the energy declines exponentially according to newly introduced D_{p2}, and additional energy variable is added to the cure depth calculation. The third stage uses the same process as the second stage, but it splits the model into n steps, where the A constant is calculated by solving an integral on each step. Additionally, D_{p2} is set as a function to laser power – the choice is clarified in Section 3.1.3. Lastly, the model is validated using real experimental data.

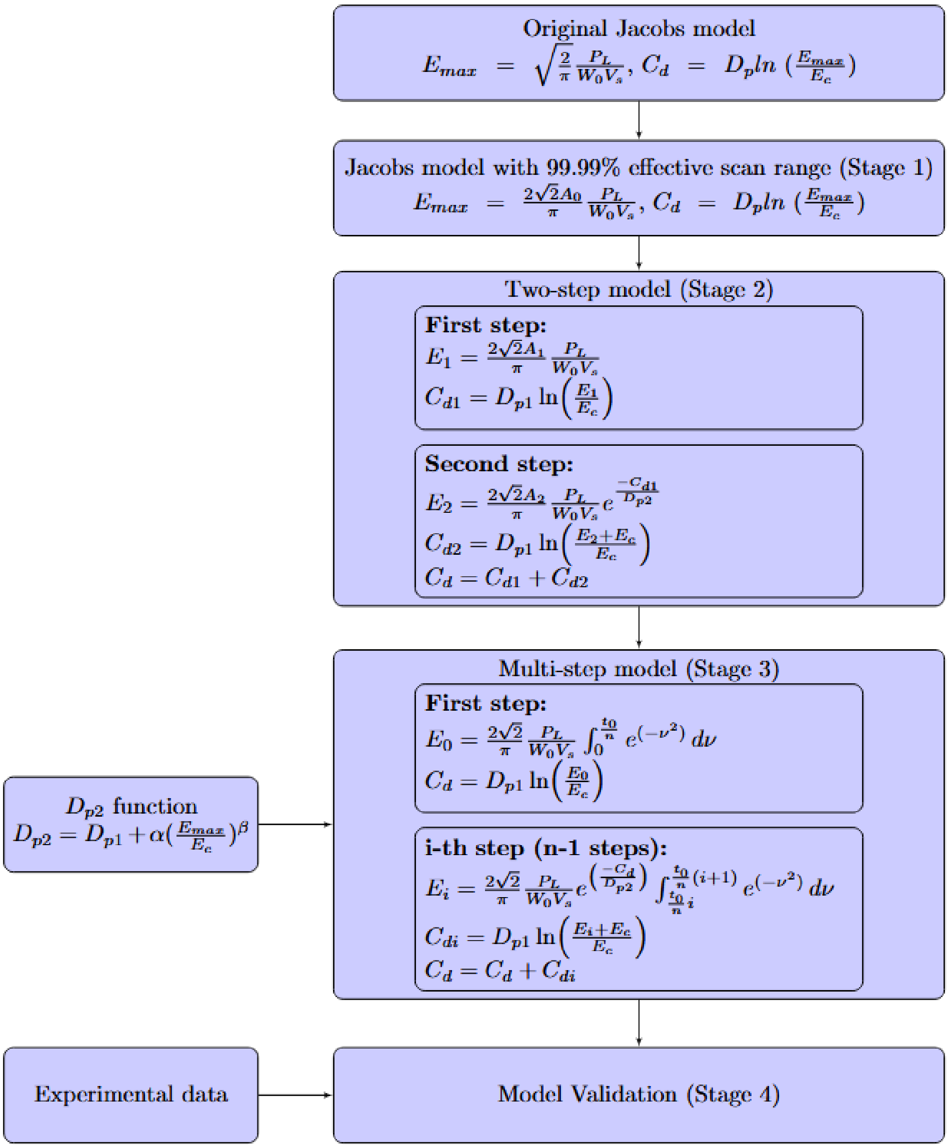

Fig. 18. Schematic of the model development

Fig. 18 shows the flow chart of the model development, which visualizes the differences between the expressions of energy E and penetration depth D_p.

3. Results

3.1. Numerical simulation of curing depth using modified model and the original model

3.1.1. Modelling identical penetration depths

Although the modified Jacobs model is theoretically consistent with original formulation, it necessary to demonstrate that both models produce identical working curves when $D_{p1} = D_{p2}$. The comparison of the two models under this assumption is shown in Fig. 19. The experimental data were taken from the WCM dataset and exhibit linear behavior at lower exposures, followed by nonlinearity at higher exposures.

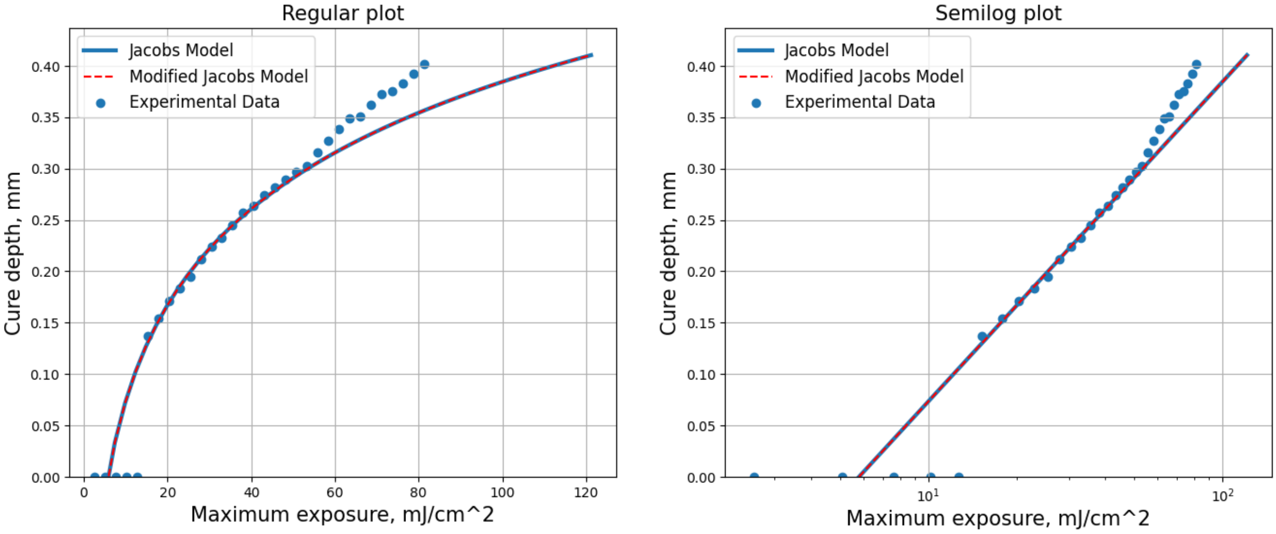

Fig. 19. Working curves of original and modified Jacobs models when $D_{p1} = D_{p2}$

Both models were evaluated using identical parameters: $W_0 = 0.01727\ cm$, $V_0 = 25.4\ cm/s$, which are typical for SLA systems [16], $P_l = 1 \dots 50\ mW$, and manually selected values of $E_c = 5.8 mJ/cm^2$ and $D_{p1} = 0.135\ mm$. The results show that modified Jacobs model aligns with the original model, indicating that the introduction of multiple steps does not alter the predicted working curve when cured and uncured photopolymer share the same penetration depth.

3.1.2. Modelling different penetration depths

Varying the penetration depth D_{p2} of the cured photopolymer does not affect original Jacobs model, but it alters the working curve predicted by the modified model, as shown in Fig. 20. In this case, the penetration depths were set to $D_{p1} = 0.135\ mm$, and $D_{p2} = 0.15\ mm$. Despite the increased penetration depth of the cured photopolymer, the resulting working curve remains linear, although with a slightly different slope and intercept compared to the Jacobs working curve.

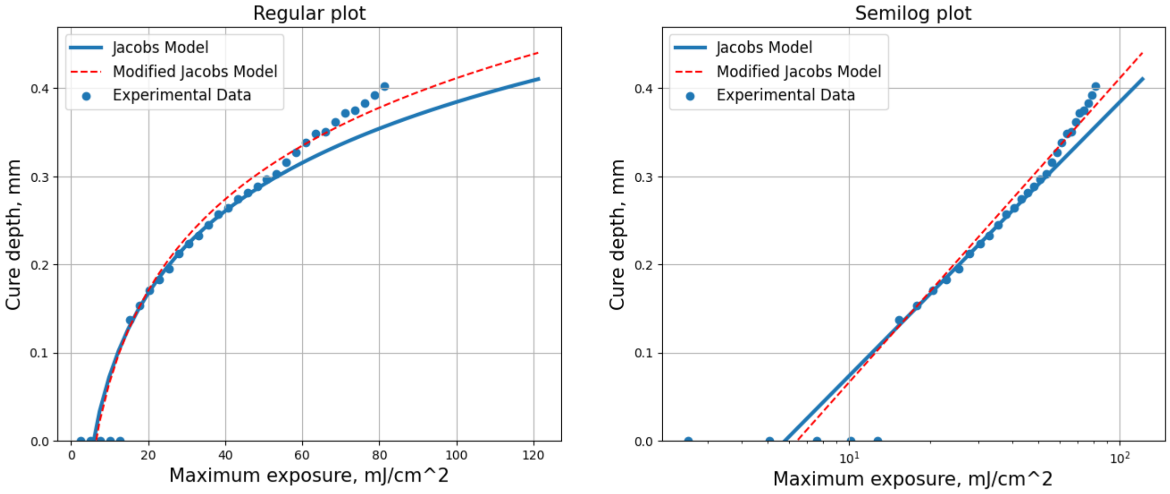

Fig. 20. Working curves of original and modified Jacobs models when $D_{p1} \neq D_{p2}$

3.1.3. Varying D_{p2} with respect to different exposures

Previous studies by Rudenko et al. and Billerbeck et al. have shown that the penetration depth and critical energy of photopolymers may vary with light intensity and wavelength [26, 21, 26], which indicate that such properties should be treated as processes-dependent empirical parameters. Under this assumption, the model can be further extended to include changes in either of these parameters under different exposure conditions.

Fig. 21 shows a comparison of the models when the penetration depth of the cured photopolymer varies according to

$$D_{p2} = D_{p1} + \alpha\left(\frac{E_{max}}{E_c}\right)^{\beta}, \tag{48}$$

where α and β are dimensionless fitting parameters. In this case, $\alpha = 0.000125$ and $\beta = 2$. The initial region of the working curve remains linear and aligns with the original Jacobs model, while deviations from linearity emerge at higher exposures. For the selected parameter values, the modified model shows good agreement with the experimental data.

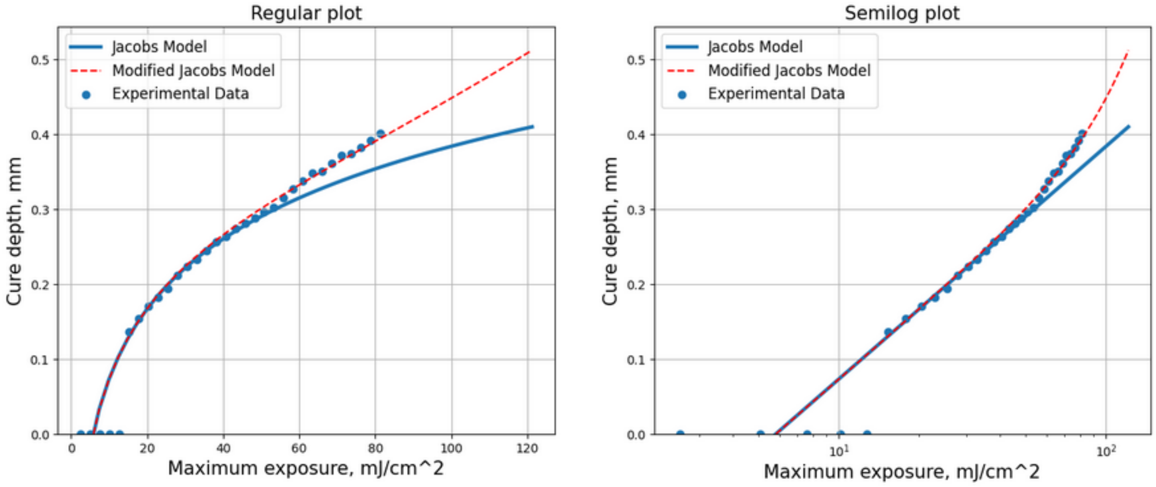

Fig. 21. Working curves of original and modified Jacobs models when D_{p2} changes dynamically

Note that in this model only D_{p2} varies with exposure, while D_{p1} and E_c remain constant. At first glance, this may appear to contradict reports that D_{p1} and E_c depend on light intensity. However, as discussed earlier, D_{p1} and E_c are empirical fitting parameters rather than intrinsic material properties. If an additional intensity or exposure dependent quantity such as D_{p2} exists but is omitted from the model, its influence can be falsely attributed to D_{p1} and E_c. This resolves the apparent contradiction: the observed intensity-dependence of D_{p1} and E_c in Jacobs model arises not because the uncured resin properties change, but because the original model omits the cured region properties, which may indeed vary with exposure.

3.1.4. Comparison between the simplified model and the full model

To evaluate whether the full model (Equations 37-41 and Equation 48) is mathematically equivalent to the simplified model (Equations 43-48), despite the different underlying assumptions, both models were evaluated using identical parameters D_{p1}, E_c, α, and β. The comparison is shown in Fig. 22. The resulting working curves overlap, indicating that the two models are mathematically equivalent under these conditions. This result suggests that the full model remains applicable even in the case of stationary laser exposure with constant power.

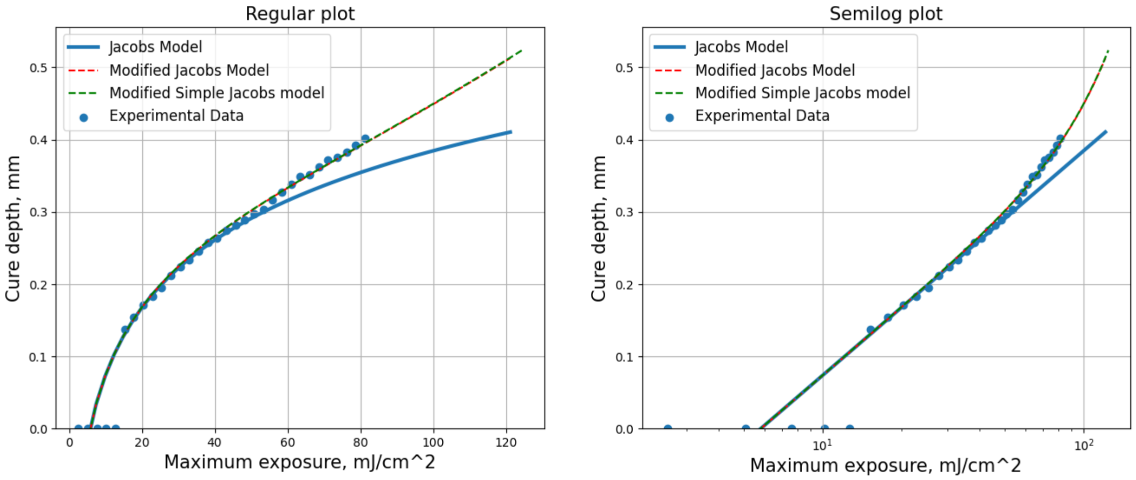

Fig. 22. Simplified model comparison with the full model

Although the working curves of the two models appear identical, the calculated exposures and cure depths are different. The ratio of the calculated exposures remains constant between models, whereas the ratio of the depths varies, as shown in Fig. 23. At lower exposures, the ratio is unstable, however, as the exposures increases, the ratio converges and stabilizes at approximately a 2% difference between the two models.

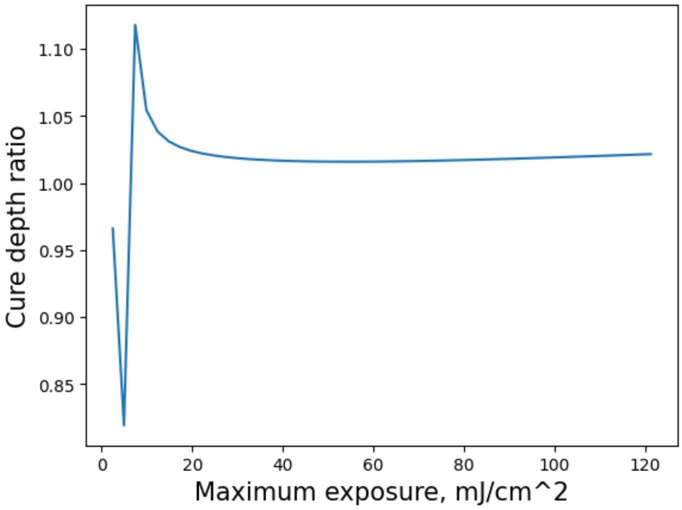

Fig. 23. Cure depth ratio of full and simplified models' dependence on exposure

3.1.5. Time step convergence

The modified model divides the curing process into multiple time steps. In the previous results, the model was evaluated using 1000 time steps; however, this choice was subjective. In principle, the model predictions should be independent of the number of steps (up to a set precision), if the process is discretized sufficiently.

To verify this, the model was tested with different time step splits, as shown in Fig. 24. As expected, using a single time step results in a linear working curve identical to the original Jacobs model. Splitting the model into two steps introduces a slight curvature at higher exposures, though the effect is minimal. At approximately 50 time steps, the working curve stabilizes, and no further changes are observed with additional time steps. Overall, the convergence of the model with increasing number of time steps indicates that the results are not dependent on the chosen discretization, thereby supporting the validity of the model.

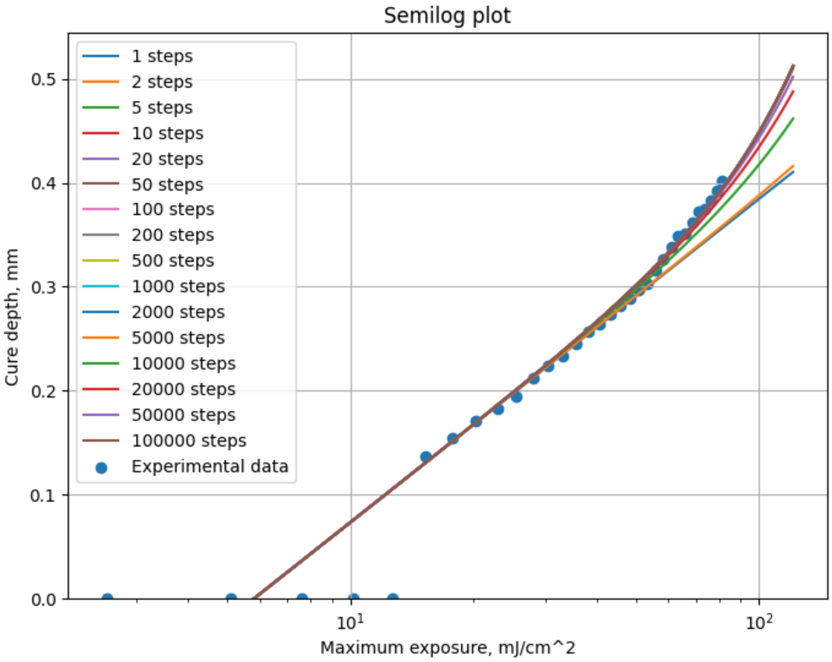

Fig. 24. Working curves of the full model with varying time step splits

3.2. Hyperparameter tuning

As discussed in Section 2.4, the model contains four parameters that must be optimized: D_{p1}, E_c, α, and β. In addition, the optimization algorithm introduces four hyperparameters that influence the fitting process:

- Initial points – the percentage of the initial experimental data points that are classified as linear data.
- Tolerance – the maximum allowable deviation from the linear model before a data point is classified as nonlinear.
- Number of particles – the number of particles used in the PySwarms algorithm.
- Number of iterations – the number of iterations performed by the PySwarms algorithm.

Because running the optimization algorithm on the full dataset can take up to one hour (with AMD Ryzen 7 3700X 3.6GHz processor and 16GB of RAM), the hyperparameters were first evaluated using a single representative experiment. The selected experiment, shown in Fig. 25, was taken from the NIST dataset and spans a wider range of exposures than a typical experiment from the WCM dataset. The hyperparameter values were chosen based on the resulting R^2 score of the model.

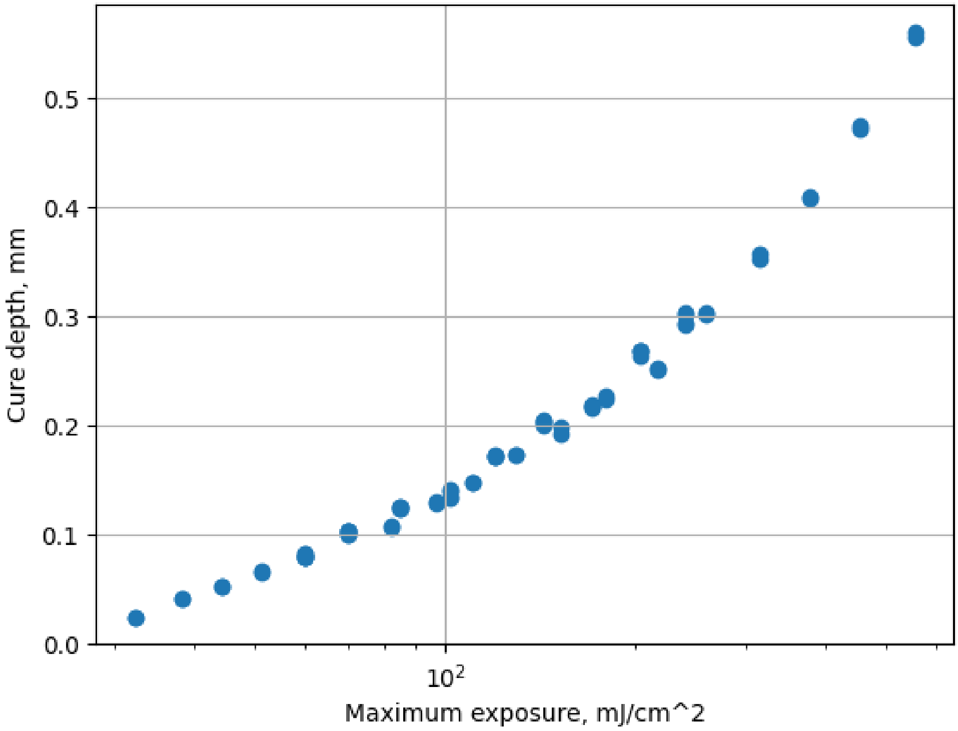

Fig. 25. A representative NIST experiment used for hyperparameter tuning

3.2.1. Initial points

The first hyperparameter investigated was the percentage of initial data points assumed to belong to the linear region of the working curve. Inspection of the datasets indicates that, for most experiments, at least the first 50% of the data is linear. However, in some cases, a larger proportion of the measurements are taken at higher exposures, resulting in smaller linear region.

In principle, selecting a smaller number of initial points provides greater flexibility for identifying the linear region. However, experimental noise and data fluctuations can bias the linear regression model when too few points are used. Increasing the number of initial data points improves robustness but reduces flexibility. Therefore, tuning this hyperparameter aims to balance flexibility and accuracy in the linear fitting stage of the algorithm.

For this analysis, the remaining hyperparameters were fixed at tolerance = 5%, number of particles = 20, and number of iterations = 20. Initial point percentages of 5%, 10%, …, 75% were tested, and the corresponding R^2 values are shown in Table 1. The highest R^2 score of 0.972 was achieved for initial point selections of 5%, 55%, 60%, 65%, and 70%. A comparable R^2 value of 0.971 was obtained for 50% and 75%, with the small difference likely attributed to the random nature of PySwarms algorithm. Based on these results, an initial point selection of 50% was chosen for the subsequent analyses, as lower percentages such as 5% are likely to be unstable across different experiments while offering no clear performance advantage.

Table 1. R^2 scores of the full model with different initial point percentages

Initial point percentage, %	R^2
5	**0.972**
10	0.951
15	0.929
20	0.951
25	0.951
30	0.951
35	0.952
40	0.951
45	0.951
50	0.971
55	**0.972**
60	**0.972**
65	**0.972**
70	**0.972**
75	0.971

3.2.2. Tolerance

The next hyperparameter investigated was the allowable error tolerance relative to the baseline linear model before a data point is classified as nonlinear. A smaller tolerance enables more precise identification of linear data points; however, experimental measurements rarely exhibit perfect linearity, and some deviation must be permitted.

For this analysis, the remaining hyperparameters were fixed at initial points = 50%, number of particles = 20, and number of iterations = 20. Tolerance values of 1%, 2%, …, 10% were tested, and their corresponding R^2 scores are shown in Table 2. The highest R^2 value of 0.971 was achieved with a tolerance of 5%, which coincided with the initial estimate.

Table 2. R^2 scores of the full model with different tolerances

Tolerance, %	R^2
1	0.934
2	0.934
3	0.951
4	0.951
5	**0.971**
6	0.970
7	0.966
8	0.966
9	0.966
10	0.966

It is noted that this optimal tolerance may differ for the WCM dataset, as the nonlinearity in those experiments is less pronounced. Consequently, a lower tolerance may be appropriate in that case, as discussed in a later section.

3.2.3. Number of particles

As noted previously, running the optimization algorithm on the full dataset can take up to an hour. One way to reduce this time is to decrease the number of particles and iterations used by the PySwarms algorithm. However, using too few particles increases the randomness of the optimization process. Therefore, an appropriate balance between computational efficiency and solution stability must be identified.

For this analysis, the hyperparameters were set as to initial points = 50%, tolerance = 5%, and number of iterations = 20, while the number of particles was varied between 5, 10, 15, 20, 25, and 30. The resulting R^2 scores are shown in Table 3. The lowest R^2 score was obtained with 5 particles, and the score increased as additional particles were introduced. However, no significant improvements were observed beyond 15 particles. Consequently, 15 particles were selected for the subsequent analyses to ensure stability, while slightly improving computational efficiency.

Table 3. R^2 scores of the full model with different number of particles

Num. particles	R^2
5	0.940
10	0.971
15	**0.972**
20	0.971
25	0.971
30	0.971

3.2.4. Number of iterations

The final hyperparameter evaluated was the number of iterations. The intent, as before, was to improve computational efficiency without compromising accuracy. For this analysis, the hyperparameters were set as initial points = 50%, tolerance = 5%, num of particles = 15, while the number of iterations was varied between 5, 10, 15, 20, 25, and 30. The R^2 scores for the corresponding number of iterations is shown in Table 4. Using only 5 iterations resulted in slightly lower accuracy compared to higher iteration counts, indicating that the algorithm converges quickly.

Table 4. R^2 scores of the full model with different number of iterations

Num. iterations	R^2
5	0.964
10	0.971
15	0.971
20	0.971
25	0.971
30	0.971

The best cost for each iteration is shown in Fig. 26. The cost converges after 8 iterations for this specific experiment. For further analysis, 10 iterations were chosen, providing a substantial improvement of computational efficiency while maintaining accuracy.

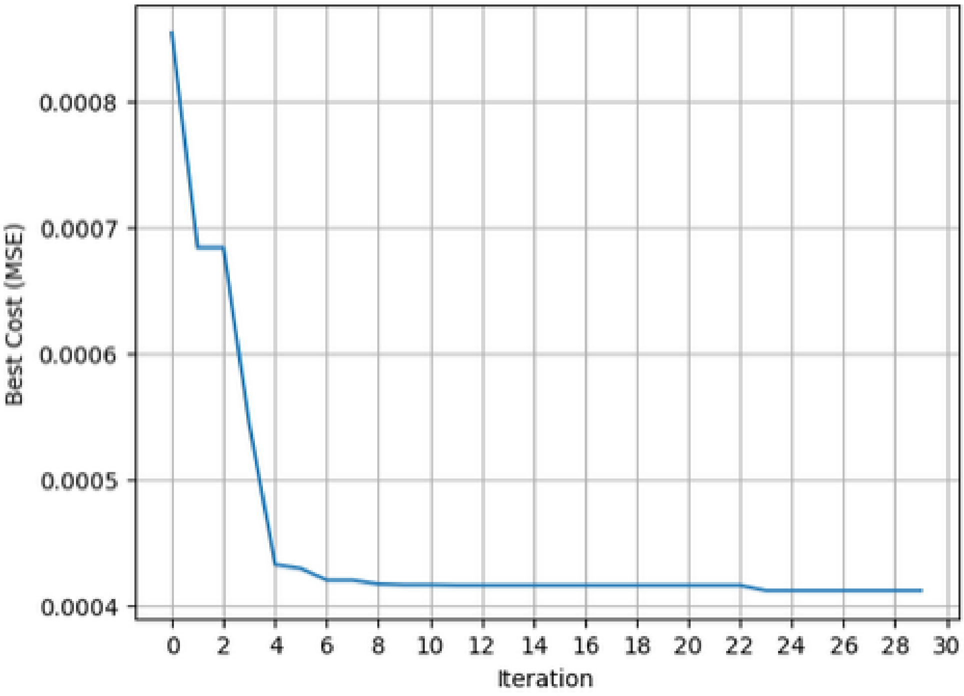

Fig. 26. Best cost convergence during hyperparameters optimization

3.2.5. Tuned hyperparameter validation

Fig. 27 shows the results of the optimization algorithm applied to the model using the selected hyperparameters of initial points = 50%, tolerance = 5%, number of particles = 15, and number of iterations = 10. While the model does not perfectly align with the nonlinear region of the experiment, as discussed earlier, no combination of tested hyperparameters yielded R^2 scores higher than 0.972.

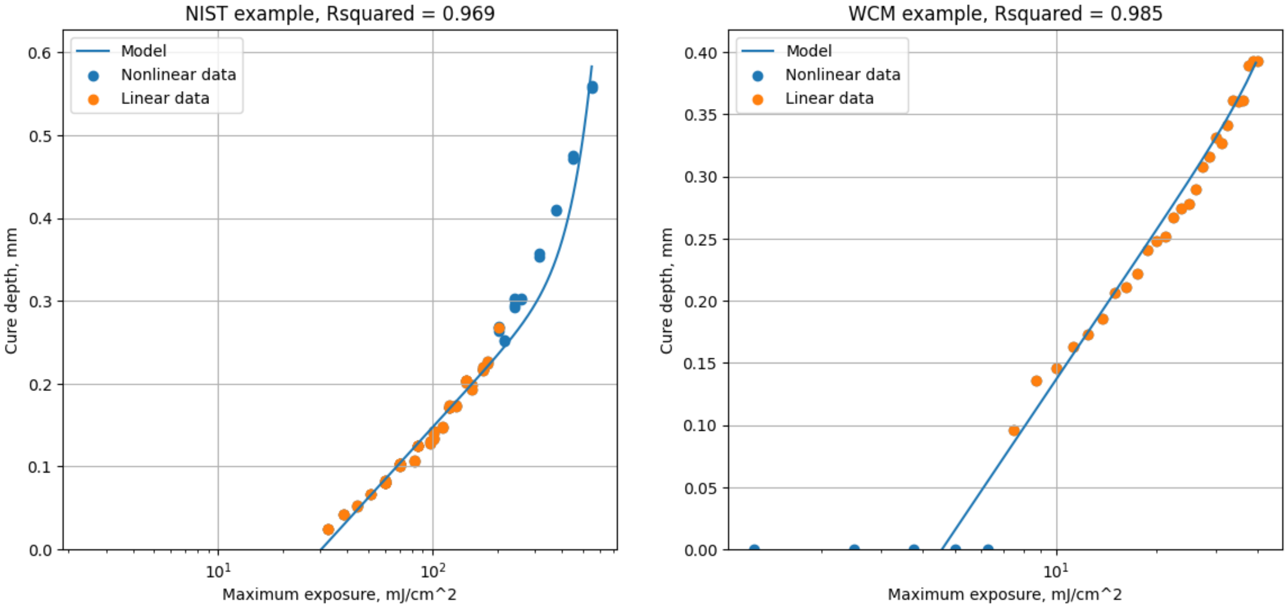

Fig. 27. Full optimization algorithm demonstration on two examples

For the WCM experiment, the model aligns well with the nonlinear region of the data. However, due to relatively high tolerance, the algorithm failed to distinguish the linear from the nonlinear portion of the data, resulting in a slight overestimation of the linear part of the function. Reducing the tolerance to 1% for the WCM experiment resolved this issue, as shown in Fig. 28, allowing the algorithm to accurately separate linear and nonlinear data and significantly improving model accuracy.

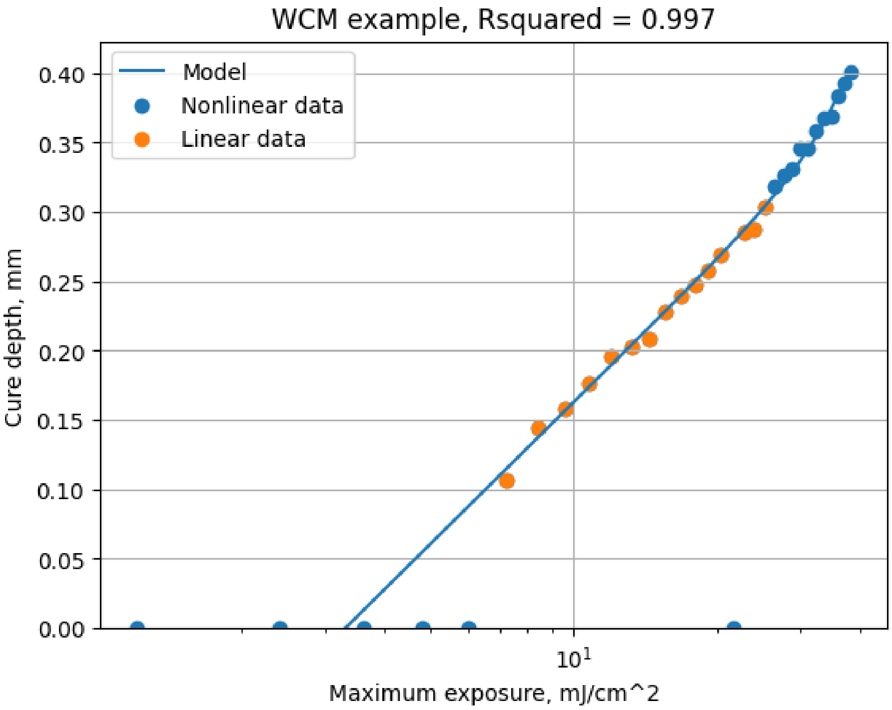

Fig. 28. Full optimization algorithm demonstration on a WCM dataset example with tolerance = 1%

As discussed in Section 2.3.1, the WCM experiments are relatively consistent with each other. Therefore, a tolerance of 1% will be used for all WCM experiments, while a tolerance of 5% is appropriate for the NIST experiments.

3.3. Optimization of the functional representation of the working curve for the full datasets

3.3.1. WCM dataset

The two-stage function fitting optimization algorithm was applied on the WCM dataset using previously tuned hyperparameters: initial points = 50%, tolerance = 1%, number of particles = 15, and number of iterations = 10. The results are shown in Fig. 29. Although the degree of nonlinearity in some experiments is subtle, the algorithm successfully segmented nonlinear regions while correctly identifying experiments that remain fully linear.

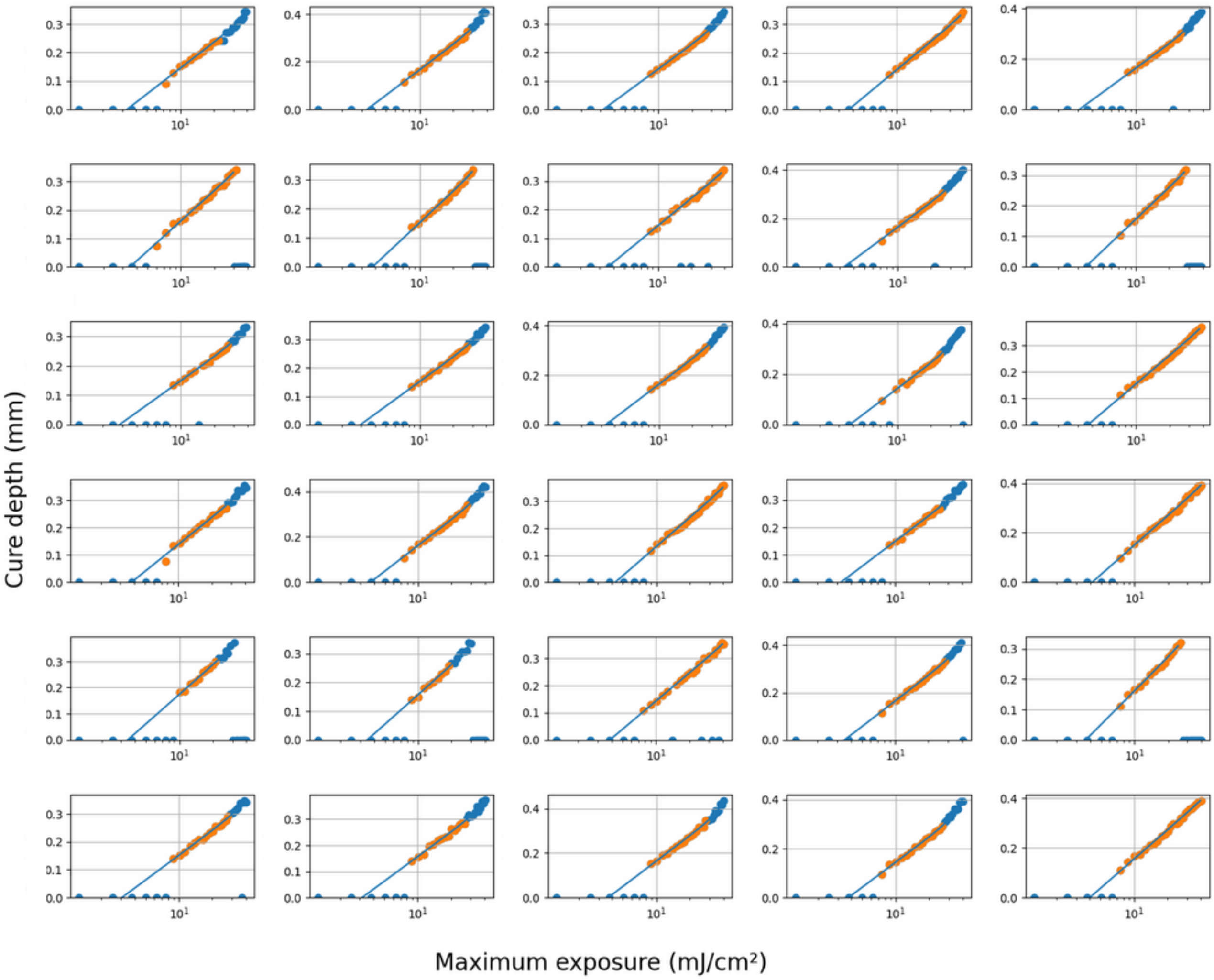

Fig. 29. Optimized functional representation of the working curves for the WCM dataset

Table 5 and Table 6 summarize the optimized parameters D_{p1}, E_c, α, and β, along with the corresponding R^2 scores for the WCM dataset. Performance of the full model was also compared against a baseline linear regression model representing the unmodified Jacobs model. In all cases, the full model was at least as accurate as the linear baseline. For fully linear experiments (Table 5), the average R^2 scores were 0.994 for the full model and 0.993 for the baseline, indicating negligible differences in accuracy.

Table 5. Linear WCM experiment parameters and accuracies of the model

Experiment	D_{p1}	E_c	α	β	R^2 (full model)	R^2 (linear model)
3	0.14	3.71	4.87e-07	3.94	**0.994**	0.992
5	0.15	3.49	3.97e-07	4.15	**0.992**	0.991
6	0.16	3.77	3.90e-07	4.64	**0.993**	0.991
7	0.14	3.56	2.49e-07	3.73	**0.994**	**0.994**
9	0.15	3.53	1.31e-07	4.80	**0.993**	**0.993**
14	0.16	3.70	2.35e-07	4.14	**0.995**	0.994
17	0.16	4.28	6.76e-08	4.97	**0.993**	0.990
19	0.17	4.18	2.13e-07	4.38	**0.995**	0.993
22	0.15	3.85	2.67e-07	3.94	**0.996**	0.994
24	0.16	3.65	4.09e-07	4.76	**0.993**	**0.993**
29	0.17	4.00	3.77e-07	3.76	**0.995**	**0.995**

In contrast, for experiments with nonlinear behavior (Table 6), the full model achieved a higher average R^2 score of 0.995 compared to 0.986 for the baseline, demonstrating a substantial improvement.

Table 6. Nonlinear WCM experiment parameters and accuracies of the model

Experiment	D_{p1}	E_c	α	β	R^2 (full model)	R^2 (linear model)
0	0.13	3.33	1.44e-07	4.53	**0.987**	0.983
1	0.15	3.39	8.56e-07	4.31	**0.996**	0.985
2	0.12	3.19	2.01e-07	4.74	**0.997**	0.987
4	0.14	3.11	9.73e-07	4.08	**0.997**	0.986
8	0.15	3.31	6.40e-07	4.40	**0.997**	0.988
10	0.12	2.82	5.80e-07	3.95	**0.997**	0.987
11	0.12	2.96	4.96e-07	4.08	**0.997**	0.990
12	0.15	3.35	8.95e-07	4.22	**0.997**	0.987
13	0.14	3.75	9.61e-07	4.70	**0.997**	0.979
15	0.14	3.79	4.76e-07	4.32	**0.992**	0.988
16	0.16	3.73	7.18e-07	4.53	**0.996**	0.988
18	0.13	3.25	5.44e-07	4.09	**0.996**	0.990
20	0.16	3.43	2.33e-07	4.75	**0.991**	0.985
21	0.15	3.49	9.52e-07	4.53	**0.992**	0.988
23	0.16	3.52	5.47e-07	4.45	**0.998**	0.990
25	0.13	3.07	9.34e-07	3.77	**0.994**	0.989
26	0.14	3.16	1.23e-07	4.69	**0.995**	0.984
27	0.16	3.68	2.22e-07	4.89	**0.996**	0.983
28	0.15	3.77	7.25e-07	4.64	**0.994**	0.981

The RMSE histograms for both models are shown in Fig. 30. Overall, the error distribution of the full model is narrower and has a lower mean compared to the linear model, indicating improved predictive accuracy. The overlap between the two histograms likely corresponds to fully linear experiments, for which both models perform similarly.

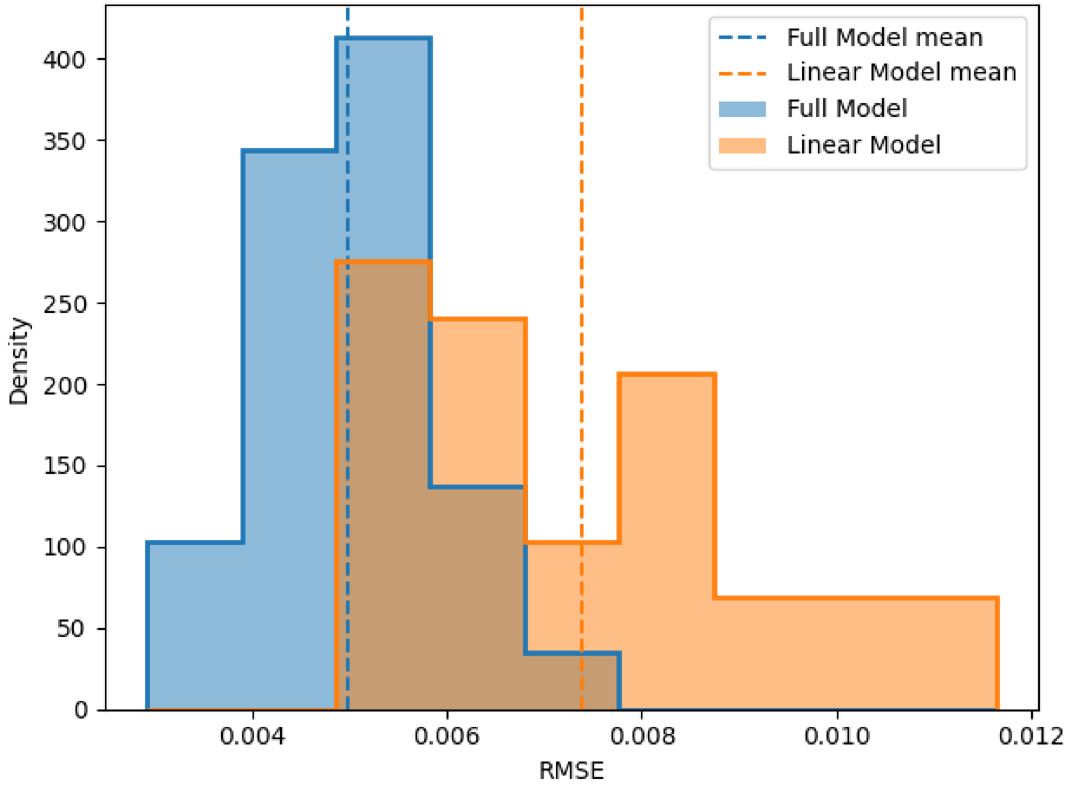

Fig. 30. RMSE histograms for the functional fitness of the models optimized on the WCM dataset

An additional consideration for the WCM dataset is model consistency. Experiments 1, 8, and 12 exhibited identical values of D_{p1} and very similar values of E_c, while the parameters α and β varied. To assess consistency, the parameters were averaged and the full model was applied to all three experiments, as shown in Fig. 31. Although the resulting function does not perfectly match the experimental data, it provides a reasonably consistent fit with R^2 scores above 0.99. This suggests that, provided D_{p1} and E_c are comparable, parameters optimized for one experiment may be used to approximate new experimental data with acceptable accuracy.

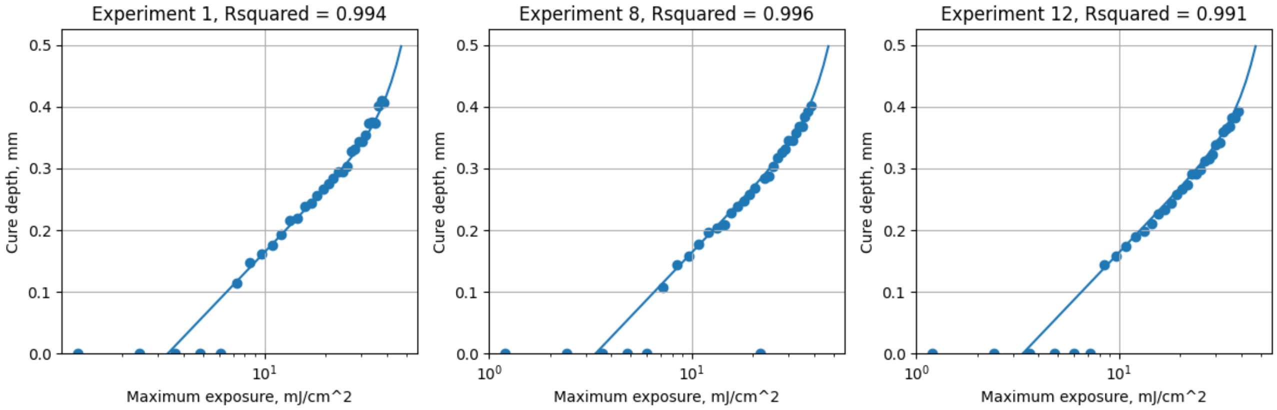

Fig. 31. Full model was tested on three similar experiments with the same parameters

3.3.2. NIST dataset

The two-stage function fitting optimization algorithm was also applied to the NIST dataset using the same hyperparameters, except for a tolerance of 5%. The results are shown in Fig. 32. As discussed previously, this dataset consists of widely varied experiments, which were useful in testing the model under different conditions. The experimental data in this dataset can be classified into three categories: linear, sub-logarithmic, and super-logarithmic behavior. For the linear cases, the algorithm correctly identifies all the data points as linear. For the super-logarithmic cases, the full model provides a reasonable fit, even when the experimental data exhibits significant variability. However, the algorithm fails to accurately capture the sub-logarithmic behavior. This outcome is not unexpected, as Jacobs did not attribute sub-logarithmic working curve behavior to optical bleaching, but instead suggested optical scattering as a plausible explanation for this phenomenon [16], which should be modeled differently compared to optical bleaching.

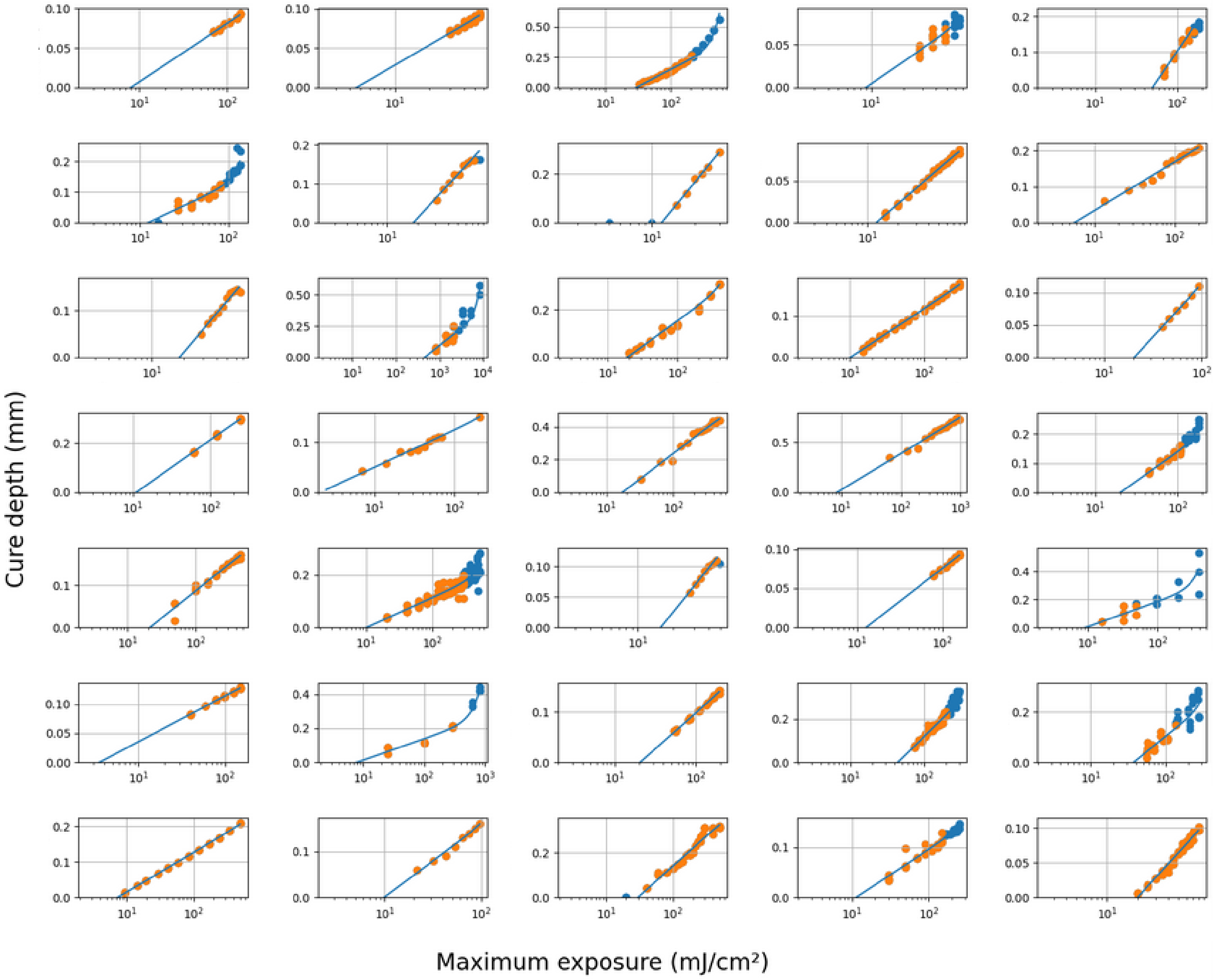

Fig. 32. Optimized functional representations of the working curves for the NIST dataset

Table 7 and Table 8 summarize the optimized parameters D_{p1}, E_c, α, and β, along with the corresponding R^2 scores for the NIST dataset. The full model was also tested against a baseline that corresponds to the Jacobs model. For experiments with linear behavior (Table 7), the accuracy of the full model is comparable to that of the baseline, with average R^2 scores of 0.982 and 0.980, respectively.

Table 7. Linear NIST experiment parameters and accuracies of the model

Experiment	D_{p1}	E_c	α	β	R^2 (full model)	R^2 (linear model)
0	0.03	8.09	1.88e-07	2.04	**0.975**	**0.975**
1	0.04	4.63	4.43e-08	3.45	**0.956**	0.924
7	0.31	11.81	-9.85e-07	4.09	**0.989**	**0.989**
8	0.05	12.41	-1.53e-07	4.30	**0.991**	**0.991**
9	0.06	5.80	-1.29e-08	2.69	**0.983**	**0.983**
10	0.12	18.13	-9.21e-07	4.95	**0.969**	0.964
12	0.09	19.05	8.38e-07	3.15	**0.980**	**0.980**
13	0.05	10.11	2.24e-07	2.43	**0.997**	**0.997**
14	0.07	20.28	8.46e-07	4.94	**0.998**	**0.998**
15	0.10	11.00	-5.22e-08	3.04	**0.997**	**0.997**
16	0.03	2.11	3.09e-07	1.71	**0.980**	**0.980**
17	0.14	17.45	-4.05e-07	2.61	**0.978**	**0.978**
18	0.16	8.54	6.23e-07	1.55	**0.979**	**0.979**
20	0.06	21.54	-3.45e-07	2.30	**0.955**	**0.955**
23	0.04	12.79	2.98e-08	3.21	**0.990**	**0.990**
25	0.03	3.53	-1.32e-08	2.11	**0.996**	**0.996**
27	0.06	20.58	1.27e-07	3.96	**0.997**	0.995
30	0.05	7.40	4.63e-07	1.79	**0.999**	**0.999**
31	0.07	9.95	3.31e-07	3.99	**0.984**	**0.982**
32	0.12	29.96	-2.29e-07	3.23	**0.958**	0.950
34	0.07	20.00	7.95e-07	4.89	**0.982**	**0.982**

For the super-logarithmic cases (Table 8), the full model provided a significant improvement, achieving an average R^2 score of 0.950 compared to 0.870 for the baseline. However, for experiments with sub-logarithmic behavior, the full model underperforms relative to the baseline, with average R^2 scores of 0.929 and 0.941, respectively.

Table 8. Nonlinear NIST experiment parameters and accuracies of the model

Experiment	D_{p1}	E_c	α	β	R^2 (full model)	R^2 (linear model)	Data type
2	0.12	30.23	8.24e-07	4.22	**0.970**	0.933	Super-Logarithmic
3	0.04	9.05	7.44e-07	4.58	**0.923**	0.773	Super-Logarithmic
4	0.15	50.52	-9.88e-07	4.92	0.942	**0.951**	Sub-Logarithmic
5	0.06	12.63	9.56e-07	4.67	**0.952**	0.841	Super-Logarithmic
6	0.12	18.33	-8.06e-07	4.90	0.919	**0.935**	Sub-Logarithmic
11	0.12	456.49	6.20e-07	4.23	**0.920**	0.881	Super-Logarithmic
19	0.09	20.40	9.58e-07	4.77	**0.962**	0.931	Super-Logarithmic
21	0.05	10.33	3.31e-07	2.71	**0.971**	0.837	Super-Logarithmic

22	0.11	15.76	-7.93e-07	4.98	0.925	**0.936**	Sub-Logarithmic
24	0.08	9.59	4.01e-07	3.18	**0.887**	0.773	Super-Logarithmic
26	0.05	8.05	1.48e-07	2.77	**0.981**	0.873	Super-Logarithmic
28	0.15	44.16	9.43e-07	4.80	**0.959**	0.947	Super-Logarithmic
29	0.11	37.50	9.95e-07	4.95	**0.945**	0.840	Super-Logarithmic
33	0.04	11.37	6.15e-07	2.80	**0.983**	0.933	Super-Logarithmic

The RMSE histograms for both models are shown in Fig. 33. Although the mean RMSE of the baseline model is slightly higher than that of the full model, the difference is less pronounced due to the large errors associated with the highly variable nature of the NIST dataset. Overall, the full model provides improved performance compared to the baseline, despite its inability to accurately capture sub-logarithmic behavior in certain experiments.

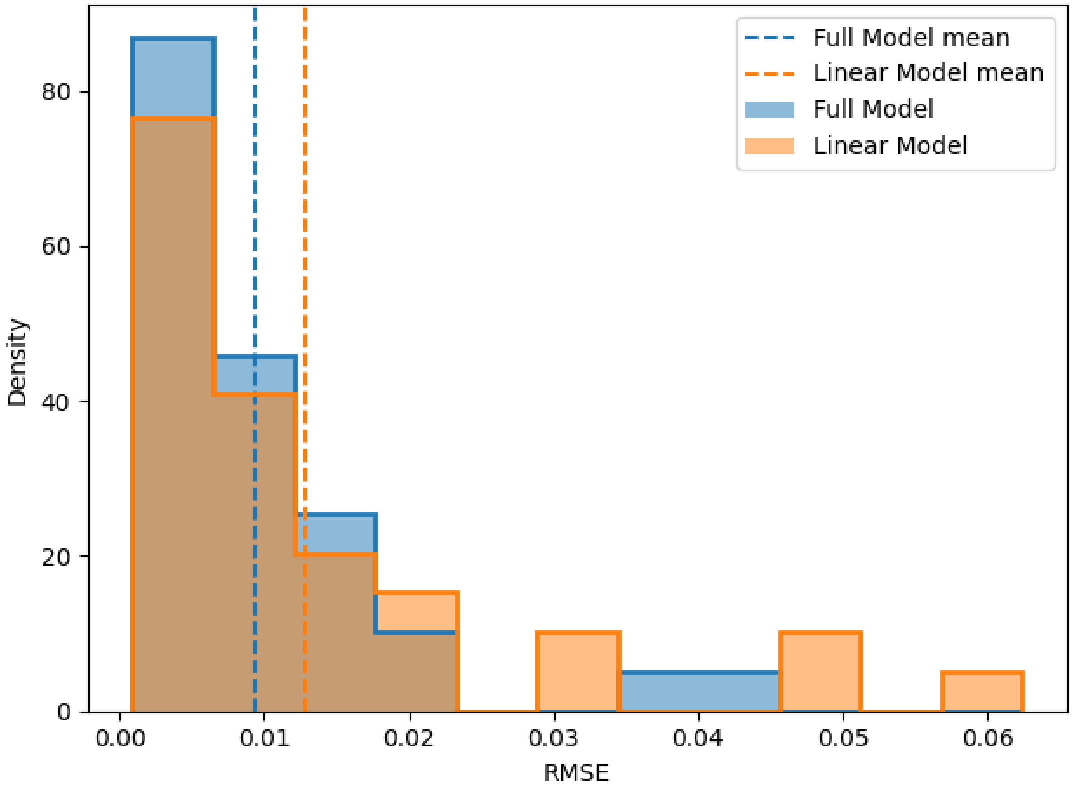

Fig. 33. RMSE histograms for the functional fitness of the models optimized on the NIST dataset

Conclusions

1. The Jacobs model for stereolithography cure depth predictions was modified by splitting the curing process into multiple steps, incorporating the properties of the cured photopolymer, which vary with different exposure conditions. This allowed to mathematically represent the effect of optical bleaching.
2. The extended model includes four parameters optimized in a two-stage process: E_c and D_{p1} are extracted from the linear portion of the data, while α and β are optimized from the full data. A constant penetration depth of the cured photopolymer D_{p2} was found to be insufficient to capture nonlinear behavior in the working curve; therefore, D_{p2} is modeled as exposure-dependent through parameters α and β.
3. The validity of the extended model was verified by comparison with the Jacobs model: when the penetration depth of the cured photopolymer is identical to the uncured photopolymer, the models align. Additionally, results are independent of the number of steps if sufficient discretization is used.
4. The extended model was tested on two datasets against a linear regression baseline. It matched the baseline for linear cases and improved average R^2 scores for super-logarithmic cases (WCM: 0.986 → 0.995; NIST: 0.870 → 0.950. For sub-logarithmic cases, the baseline outperformed the extended model, indicating that optical bleaching is effectively captured only in linear and super-logarithmic regimes.
5. Model consistency was evaluated for the WCM dataset by applying the same parameters for three similar experiments. The results showed reasonably accurate fits, with R^2 scores over 0.99, suggesting that α and β parameters are stable under comparable conditions.

List of references

1. CHUA, C.K., LEONG, K.F. and AN, J. Rapid prototyping of biomaterialsElsevier Ltd, 2014 *1 - Introduction to Rapid Prototyping of Biomaterials*, pp. 1–15.

2. SATYANARAYANA, B. and PRAKASH, K.J. Component Replication using 3D Printing Technology. *Procedia Materials Science*, 2015, vol. 10. pp. 263–269.

3. HOLMSTRÖM, J., PARTANEN, J., TUOMI, J. and WALTER, M. Rapid Manufacturing in the Spare Parts Supply Chain. *Journal of Manufacturing Technology Management*, Jan 1, 2010, vol. 21, no. 6. pp. 687–697.

4. HASAN, Z. *Tooling for Composite Aerospace Structures.* 1st ed. San Diego, CA, USA: Elsevier Science, 2020

5. CRAVEIRO, F., DUARTE, J.P., BARTOLO, H. and BARTOLO, P.J. Additive Manufacturing as an Enabling Technology for Digital Construction: A Perspective on Construction 4.0. *Automation in Construction*, Jul, 2019, vol. 103. pp. 251–267.

6. KLENAM, D.E.P., et al. Additive Manufacturing: Shaping the Future of the Manufacturing Industry – Overview of Trends, Challenges and Opportunities. *Applications in Engineering Science*, Jun, 2025, vol. 22. pp. 100224.

7. ZHOU, L., et al. Additive Manufacturing: A Comprehensive Review. *Sensors*, Apr 23, 2024, vol. 24, no. 9. pp. 2668.

8. DESHMANE, S., KENDRE, P., MAHAJAN, H. and JAIN, S. Stereolithography 3D Printing Technology in Pharmaceuticals: A Review. *Drug Development and Industrial Pharmacy*, Sep 2, 2021, vol. 47, no. 9. pp. 1362–1372.

9. HUSNA, A., et al. Recent Advancements in Stereolithography (SLA) and their Optimization of Process Parameters for Sustainable Manufacturing. *Hybrid Advances*, Dec, 2024, vol. 7. pp. 100307.

10. HULL C. Apparatus for Production of Three-Dimensional Objects by Stereolithography. *U.S. Patent no. 4,575,330*, 1986 CiNII Research of NDL.

11. HUANG, J., QIN, Q. and WANG, J. A Review of Stereolithography: Processes and Systems. *Processes*, Sep 1, 2020, vol. 8, no. 9. pp. 1138.

12. CRIVELLO, J.V. and REICHMANIS, E. Photopolymer Materials and Processes for Advanced Technologies. *Chemistry of Materials*, Jan 14, 2014, vol. 26, no. 1. pp. 533–548.

13. MSALLEM, B., et al. Dimensional Accuracy in 3D Printed Medical Models: A Follow-Up Study on SLA and SLS Technology. *Journal of Clinical Medicine*, Oct 1, 2024, vol. 13, no. 19. pp. 5848.

14. VASAMSETTY, P., et al. 3D Printing in Dentistry – Exploring the New Horizons. *Materials Today : Proceedings*, Jan 1, 2020, vol. 26. pp. 838–841.

15. TRIACCA, A., et al. Stereolithography 3D Printed Implants: A Preliminary Investigation as Potential Local Drug Delivery Systems to the Ear. *International Journal of Pharmaceutics*, Mar 25, 2022, vol. 616. pp. 121529.

16. JACOBS, P.F. *Rapid Prototyping & Manufacturing.* 1. ed., 4. print. ed. Dearborn, Mich: Soc. of Manufacturing Engineers, 1992.

17. BODDAPATI, A. *Modeling Cure Depth during Photopolymerization of Multifunctional Acrylates.* Georgia Institute of Technology, Jun 10, 2010.

18. JARIWALA, A.S., et al. Modeling Effects of Oxygen Inhibition in Mask-Based Stereolithography. *Rapid Prototyping Journal*, Apr 26, 2011, vol. 17, no. 3. pp. 168–175.

19. BLYWEERT, P., NICOLAS, V., FIERRO, V. and CELZARD, A. Numerical Simulation Model for the Curing of Photosensitive Acrylate Resin in a Stereolithography Process. *International Journal of Advanced Manufacturing Technology*, Dec 1, 2024, vol. 135, no. 11. pp. 5157–5172.

20. ZHAKEYEV, A., ZHANG, L. and XUAN, J. 3D and 4D Printing of Polymer Nanocomposite MaterialsElsevier Inc, 2020 *Chapter 13 - Photoactive Resin Formulations and Composites for Optical 3D and 4D Printing of Functional Materials and Devices*, pp. 387–425.

21. RUDENKO, Y., et al. Light Intensity Influence on Critical Energy and Penetration Depth for Vat Photopolymerization Technology. *Progress in Additive Manufacturing*, Apr, 2024, vol. 9, no. 2. pp. 553–561.

22. OSHINA, I. and SPIGULIS, J. Beer–Lambert Law for Optical Tissue Diagnostics: Current State of the Art and the Main Limitations. *Journal of Biomedical Optics*, Oct 1, 2021, vol. 26, no. 10. pp. 100901.

23. GOLDSMITH, P.F. *Quasioptical Systems.* Piscataway, NJ: IEEE Press, 1998.

24. WEI, Y., LIU, X., PARK, S. and TOMKOWSKI, R. A Study of Micro-Dimpled Groove Texture in Friction Reduction. *Micromachines*, Mar, 2021.

25. BENNETT, J. Measuring UV Curing Parameters of Commercial Photopolymers used in Additive Manufacturing. *Additive Manufacturing*, Dec 1, 2017, vol. 18. pp. 203–212.

26. BILLERBECK, K., HÄGELE, C. and TRÄGER, J. Relation of the Working Curve and Exposure Intensity in VPP 3D-Printing. *Progress in Additive Manufacturing*, Aug, 2024, vol. 9, no. 4. pp. 1015–1023.

27. HOYLE, C.E., et al. *Radiation Curing of Polymeric Materials.* 1st ed. Washington, DC: American Chemical Society, 1990.

28. GIBSON, I., ROSEN, D., STUCKER, B. and KHORASANI, M. *Additive Manufacturing Technologies.* Third edition ed. Cham: Springer, 2021.

29. PANANAKIS, D. and WATTS, D.C. Incorporation of the Heating Effect of the Light Source in a Non-Isothermal Model of a Visible-Light-Cured Resin Composite. *Journal of Materials Science*, Sep 1, 2000, vol. 35, no. 18. pp. 4589–4600.

30. LEE, S.H., et al. A Neural Network Approach to the Modelling and Analysis of Stereolithography Processes. *Proceedings of the Institution of Mechanical Engineers. Part B, Journal of Engineering Manufacture*, Dec 1, 2001, vol. 215, no. 12. pp. 1719–1733.

31. KARALEKAS, D. and AGGELOPOULOS, A. Study of Shrinkage Strains in a Stereolithography Cured Acrylic Photopolymer Resin. *Journal of Materials Processing Technology*, May 10, 2003, vol. 136, no. 1. pp. 146–150.

32. GUO, X., et al. Multi-Objective Optimization on the Parameters of Variable Laser Spot for the SL Printing with a New Path Planning Algorithm. *Journal of Mechanical Science and Technology*, Dec, 2024, vol. 38, no. 12. pp. 6859–6872.

33. MANDRYCKY, C., WANG, Z., KIM, K. and KIM, D. 3D Bioprinting for Engineering Complex Tissues. *Biotechnology Advances*, Jul 1, 2016, vol. 34, no. 4. pp. 422–434.

34. YU, Y., ZHANG, Y., MARTIN, J.A. and OZBOLAT, I.T. Evaluation of Cell Viability and Functionality in Vessel-Like Bioprintable Cell-Laden Tubular Channels. *Journal of Biomechanical Engineering*, Sep 1, 2013, vol. 135, no. 9. pp. 91011.

35. XU, H., et al. Prediction of Cell Viability in Dynamic Optical Projection Stereolithography-Based Bioprinting using Machine Learning. *Journal of Intelligent Manufacturing*, Nov, 2020, vol. 33, no. 4. pp. 995–1005.

36. KILLGORE, J.P., et al. A Data-Driven Approach to Complex Voxel Predictions in Grayscale Digital Light Processing Additive Manufacturing using U-Nets and Generative Adversarial Networks. *Small (Weinheim an Der Bergstrasse, Germany)*, Dec 1, 2023, vol. 19, no. 50. pp. 2301987.

37. CHAUDHARY, R., et al. Additive Manufacturing by Digital Light Processing: A Review. *Progress in Additive Manufacturing*, Apr, 2023, vol. 8, no. 2. pp. 331–351.

38. BOHLIN, T. *Practical Grey-Box Process Identification : Theory and Applications.* 1st ed. London: Springer London, 2006.

39. SOHLBERG, B. and JACOBSEN, E.W. Grey Box Modelling – Branches and Experiences. *IFAC Proceedings Volumes*, 2008, vol. 41, no. 2. pp. 11415–11420.

40. LI, Y., et al. Grey-Box Modeling and Application for Building Energy Simulations - A Critical Review. *Renewable & Sustainable Energy Reviews*, Aug 1, 2021, vol. 146. pp. 111174.

41. CRESPO, R.N.F., et al. *A Distributed Software Platform for Additive Manufacturing.* Piscataway: IEEE, Sep 12, 2023.

42. TAMIR, T.S., XIONG, G., SHEN, Z. and LENG, J. Physics-Driven Data Collection in 3-D Printing: Traversing the Realm of Social Manufacturing. *IEEE Transactions on Computational Social Systems*, Dec 1, 2024, vol. 11, no. 6. pp. 7909–7928.

43. KOLIBABA, T.J. and KILLGORE, J.P. *Raw Data from NIST-Led Interlaboratory Study on the Working Curve in Vat Photopolymerization.* National Institute of Standards and Technology, 2023 Available from: https://commons.datacite.org/doi.org/10.18434/mds2-3137.